



20160329016

**REPORT DOCUMENTATION PAGE**

*Form Approved  
OMB No. 0704-0188*

The public reporting burden for this collection of information is estimated to average 1 hour per response, including the time for reviewing instructions, searching existing data sources, gathering and maintaining the data needed, and completing and reviewing the collection of information. Send comments regarding this burden estimate or any other aspect of this collection of information, including suggestions for reducing the burden, to Department of Defense, Washington Headquarters Services, Directorate for Information Operations and Reports (0704-0188), 1215 Jefferson Davis Highway, Suite 1204, Arlington, VA 22202-4302. Respondents should be aware that notwithstanding any other provision of law, no person shall be subject to any penalty for failing to comply with a collection of information if it does not display a currently valid OMB control number.  
**PLEASE DO NOT RETURN YOUR FORM TO THE ABOVE ADDRESS.**

1. REPORT DATE (DD-MM-YYYY) 03/15/2016		2. REPORT TYPE Final Technical Report		3. DATES COVERED (From - To) 15-06-2013 to 15-12-2015	
4. TITLE AND SUBTITLE Control of Supercavitating Vehicles using Transverse Jets				5a. CONTRACT NUMBER	
				5b. GRANT NUMBER N00014-13-1-0747	
				5c. PROGRAM ELEMENT NUMBER	
6. AUTHOR(S) Ayers, Bradley and Johari, Hamid				5d. PROJECT NUMBER	
				5e. TASK NUMBER	
				5f. WORK UNIT NUMBER	
7. PERFORMING ORGANIZATION NAME(S) AND ADDRESS(ES) Mechanical Engineering Department California State University, Northridge Northridge, CA 91330				8. PERFORMING ORGANIZATION REPORT NUMBER	
9. SPONSORING/MONITORING AGENCY NAME(S) AND ADDRESS(ES) Office of Naval Research 875 North Randolph Street Arlington, VA 22203-1995				10. SPONSOR/MONITOR'S ACRONYM(S) ONR	
				11. SPONSOR/MONITOR'S REPORT NUMBER(S)	
12. DISTRIBUTION/AVAILABILITY STATEMENT Approved for public release; distribution is unlimited.					
13. SUPPLEMENTARY NOTES					
14. ABSTRACT The primary objective of this experimental study was to investigate the effects of high freestream velocity and an upstream ventilated cavity on the loads generated by a zero-net-mass-flux thruster operating in an aqueous environment. In the absence of freestream flow, averaged thrust increased linearly with frequency, up to a limit imposed by the hardware response time. A simple model was developed that predicts thrust to scale linearly with operating frequency and expelled fluid slug stroke ratio. Thrust decreased with increasing crossflow velocity, and this decrease was linear for the range of frequencies less than or equal to 16 Hz. Thruster performance was diminished when a ventilated cavity was present.					
15. SUBJECT TERMS zero-net-mass-flux thruster, jet in crossflow					
16. SECURITY CLASSIFICATION OF:			17. LIMITATION OF ABSTRACT	18. NUMBER OF PAGES	19a. NAME OF RESPONSIBLE PERSON
a. REPORT	b. ABSTRACT	c. THIS PAGE			19b. TELEPHONE NUMBER (Include area code)
U	U	U	SAR	50	

**CONTROL OF SUPERCAVITATING VEHICLES USING  
TRANSVERSE JETS**

**Final Technical Report**

**for Office of Naval Research contract N00014-13-1-0747**

**covering the period June 15, 2013 to December 15, 2015**

**Bradley Ayers and Hamid Johari**

Mechanical Engineering Department  
California State University, Northridge  
Northridge, CA 91330

Tel: (818) 677-3099  
Fax: (818) 677-7062  
email: [hjohari@csun.edu](mailto:hjohari@csun.edu)

**Administrative Representative for California State University, Northridge**

Scott Perez, Director  
Research and Sponsored Projects  
University Hall 265, Mail Drop: 8232  
California State University, Northridge  
Northridge, CA 91330

Tel: (818) 677-2901  
Fax: (818) 677-4691  
email: [scott.perez@csun.edu](mailto:scott.perez@csun.edu)

20160329016

## SYNOPSIS

The primary objective of this experimental study was to investigate the effects of high freestream velocity and an upstream ventilated cavity on the forces and moments generated by a zero-net-mass-flux thruster operating in an aqueous environment. This work was motivated by the desire to generate meaningful turning moments on a fully-submerged, supercavitating vehicle model using the thrust of the zero-net-mass-flux device. The experiments were conducted in NUWC Newport's research water tunnel facility, and the vehicle model was a sting-mounted, 3-inch diameter cylindrical body connected to a 6-axis waterproof load cell. The zero-net-mass-flux thruster was contained within the model, with the orifice located near the aft end and oriented perpendicular to the tunnel flow. The thruster consisted of a high-impulse solenoid driving a piston in a cylindrical cavity. The Reynolds number based on the thruster characteristic velocity and the orifice diameter was 63,000. The time averaged net forces and moments on the model were measured for thruster operating frequencies up to 24 Hz and tunnel velocities of up to 8 m/s. For ventilated cavity experiments, ventilation rates were also varied.

In the absence of freestream flow in the tunnel, time averaged thrust increased linearly with frequency, up to a limit (16 Hz) imposed by the solenoid response time. A simple model was developed that predicts thrust to scale linearly with operating frequency and expelled fluid slug stroke ratio, consistent with the measurements in the quiescent ambient case.

The time averaged thrust decreased with increasing crossflow (freestream) velocity, and this decrease was linear for the range of frequencies less than or equal to 16 Hz. An expression was developed to allow the estimation of net thrust as a function of the thruster operating parameters and crossflow velocity for crossflow velocities as high as the thruster characteristic velocity. The decrease in thrust with increasing crossflow velocity is attributed to secondary vortex structures, formed during the expulsion phase, and the accompanying low pressure areas on the surface of the model vehicle. The thruster performance was severely inhibited by the ingestion of air bubbles in the cases with a ventilated cavity that closed upstream of the thruster orifice.

## Introduction

Maximum speed is an important consideration in the design of underwater vehicles. In the past several decades the use of supercavitation as a viable means of drastically reducing drag on underwater vehicles has been proposed and demonstrated, thus allowing for considerably greater maximum speeds. Even though significant research had been carried out on supercavitation, there are still challenges associated with effectively and reliably controlling supercavitating vehicles. Thus it was proposed to examine the viability of transverse jets as a means of creating turning moments for maneuvering purposes.

The last decade has seen the implementation of zero-net-mass-flux (ZNMF) jet actuators in a variety of real-world applications. These actuators produce ‘synthetic’ jets through periodic ingestion and expulsion of the surrounding fluid (James et al. 1996; Smith & Glezer 1998; Glezer & Amitay 2002). This two-phase cycle consists of an ingestion phase wherein fluid is drawn into a cavity through an orifice from all directions. Following this, the fluid is forcefully ejected from the orifice along the axis. In this process, a toroidal vortex is produced carrying momentum normal to the plane of the orifice and thus imparting a force without the need for a pressurized reservoir or any plumbing. The flow field in the near field of ZNMF actuators with both rectangular and round orifice geometries has been examined previously (Cater & Soria 2002; Buren et al. 2014).

Several common methods have been employed to produce the periodic motion required to produce the synthetic jet. The electromechanical method of choice has varied with respect to the working fluid and the specific aim of the study. Extensive work has been conducted on the cooling capabilities of ZNMF actuators (Kercher et al. 2003; Mahalingam et al. 2004; Chaudhari et al. 2010) which are typically achieved through the use of piezoelectric elements. The most prominent utilization of ZNMF actuators has been in the field of flow control, typically in the context of separation control and stall delay on airfoils (Amitay & Glezer 2002; Maldonado et al. 2009; Mejia et al. 2011; Woo & Glezer 2013; Vasile & Amitay 2015) but also more generally with other flow fields (Tamburello & Amitay 2008; Gezer 2011; DeMauro et al. 2013). These applications have employed piezoelectric elements which are well suited for flows where the working fluid is air and high frequency actuation is required.

In aqueous applications, more robust mechanisms are needed to accommodate the substantial density of water. Additionally, the actuation frequencies are necessarily lower due to

the onset of cavitation at higher frequencies. Most commonly, aqueous ZNMF actuators have been driven by voice coils (Polisenburg-Thomas et al. 2005), motors and cams (Kreig et al. 2005; Mohseni 2006; Kreig & Mohseni 2008), and a high-impulse solenoid (Ayers 2015). The primary focus of studies on ZNMF actuator in water has been the production of thrust for low-speed propulsion and maneuvering of underwater vehicles. This was also the motivation for the current research where an attempt was made to create meaningful turning moments on a fully-submerged model vehicle from the thrust of a ZNMF device for maneuvering purposes.

Given that ZNMF thrusters create distinct vortex rings in the near field, previous fundamental studies on pulsed jets in crossflow and on the interaction of distinct vortex rings with crossflow (Chang & Vakili 1995; Eroglu & Breidenthal 2001; M'Closkey et al. 2002; Johari 2006; Sau & Mahesh 2008) may be used to explore the underlying physical phenomena. Direct numerical simulation at relatively low Reynolds numbers has indicated that a coherent vortex ring does not form when the average orifice velocity is less than twice the freestream velocity (Sau & Mahesh 2008). This has been attributed to the crossflow boundary layer vorticity inhibiting the roll-up of the vorticity emerging from the orifice. For average orifice velocity exceeding the minimum value of twice the freestream velocity, a distinct vortex forms up to a stroke ratio 3.5 to 4. Beyond this stroke ratio, a trailing jet follows the vortex ring. This is consistent with the notion of vortex ring formation number in quiescent surroundings first observed by Gharib et al. (1998). Even for the case of a steady jet in crossflow, jet-to-crossflow velocity ratios of less than two result in a different vortex structure in the near field (Gopalan et al. 2004).

The goal of this experimental study was to measure the thrust and flow field of a high Reynolds number jet created by a custom-designed ZNMF thruster in aqueous crossflow. The thruster was operated at frequencies up to 24 Hz with a duty cycle of 0.3 and the crossflow velocity was varied up to 8 m/s. The Reynolds number based on the orifice diameter and the characteristic velocity of expulsion was 63,000. The time averaged thrust is reported as a function of actuation frequency and crossflow velocity with and without a ventilated cavity upstream of the thruster orifice.

## Experimental Technique

All experiments reported here were conducted at the Naval Undersea Warfare Center (NUWC) closed loop research water tunnel in Newport, RI. The tunnel test section is 12-in square with glass side walls, and freestream speeds of up to 30 ft/s are possible in the test section. The freestream turbulent intensity on the tunnel centerline was measured to be in the range of 0.6% to 1.0% for the freestream velocities considered. During the experiments the freestream velocity was recorded using a pitot tube located in the freestream at the same cross-sectional plane as the thruster orifice. In this manner, the increase in local freestream velocity caused by partial tunnel blockage was accounted for, and it was thus ensured that recorded crossflow velocities would accurately reflect the conditions at the thruster location.

### Model and Thruster Design

The aim of model design and construction was to create an analog of a high-speed underwater vehicle, i.e. a streamlined, axisymmetric body of length about ten times its diameter. The bulk of the vehicle length was a simple hollow aluminum tube with the aft section containing a watertight module housing the ZNMF thruster subassembly. The thruster orifice was flush with the vehicle surface with an orifice to hull diameter of 1:6. The model was constrained to occupying no more than 5% of the cross-sectional area of the water tunnel test section to minimize any tunnel blockage issues. With the nominal test section of 12-in square, this limited the model diameter to 3 in. It was considered desirable from the design standpoint to make the vehicle this maximum diameter to offer as much space as possible for the internal ZNMF thruster components. The model shown in Fig. 1 was sting mounted to minimize any upstream disturbances outside the boundary layer.



Fig. 1. The vehicle model with the enclosed ZNMF thruster. The orifice is near the aft section.

The ZNMF thruster was designed to produce the greatest force possible given the tight size constraints. Because there was no restriction on the axial length of the thruster subassembly, it was decided that the driving mechanism should be oriented axially within the model. This was a departure from most previous setups discussed in literature wherein the flow had been driven by bellows or a piston in the same direction as the orifice. It was assumed that if the ratio of piston to orifice area was adequately large, secondary flow within the chamber across the orifice will be sufficiently small such that it will not significantly influence the velocity profile of exiting fluid. Velocity field measurements under quiescent conditions supported this assumption.

The thruster in the setup was driven by a high-impulse solenoid rather than by a motor and cam combination as used in previous work on ZNMF thrusters operating in aqueous environment. Perhaps the most significant advantage to a solenoid is its compactness, which allows it to fit into the vehicle model with relative ease. The solenoid is also simple to operate insofar as it requires minimal signal processing to control its motion; all that is needed is a square-wave with desired voltage, frequency, and duty cycle. The selected model was a Ledex Low Profile 6EC which was the strongest of a class of high-impulse solenoids that would fit in the available space in the model. Because the solenoid data sheet showed rapid decrease in force as the plunger moved farther from the de-energized position, there was added incentive to keep the stroke length of the plunger as short as possible. The solenoid specifications indicated that stroke lengths less than 5.0 mm would have stroke times  $\sim 10$  ms. For all the experiments carried out, the ZNMF thruster was operated by a square wave with a 30% duty cycle. A function generator was used to produce the signal which was then amplified externally. The power supplied to the solenoid was current-source limited to 10 A.

The thruster design was driven by the solenoid characteristics and a model of the system which is briefly described in the following paragraph. In the interest of keeping the stroke length short, a stroke length of only 4 mm and a cylinder bore of 45 mm was chosen for the thruster. For a 12.7 mm (0.5 in) orifice diameter, this configuration resulted in a 49.8 mm fluid slug during the outstroke. The stroke ratio, or the length-to-diameter ratio, of the ideal fluid slug was 3.92. This ratio, which is also referred to as the formation number, is in the middle of the optimum range for vortex ring formation as suggested by Gharib et al. (1998).

A cutaway of the ZNMF thruster subassembly as well as the assembled thruster is shown in Fig. 2. The collinear piston, plunger, and return spring bolt near the centerline of the assembly constituted the moving parts. The solenoid (in blue) held the piston in the fully extended position by keeping the plunger pulled tightly in the energized position. When the solenoid circuit was opened, the return spring housed between the backstop plate and return spring bolt pulled the moving parts downward until the plunger contacted the backstop plate and the fully de-energized position was reached. The thruster orifice had a 30-deg internal bevel to reduce any flow reversal on the outstroke. The critical dimensions of the thruster cavity and the fluid slug are shown in Fig. 3.

Using the solenoid characteristics, a nonlinear ordinary differential equation was developed to assist in determining optimal design parameters such as the stroke length, piston diameter, and the orifice diameter. In

development of this model, three separate elements were considered. The first of these was the fluid inertia within the chamber being driven by the piston, in addition to the mass of moving parts of the assembly. The second element considered was the loss term associated with flow restriction across the orifice which was modeled by the pressure drop of an orifice plate. Finally, the force of the return spring in opposition to the solenoid force was taken into account. The thruster model which is described in more detail in Ayers (2015) was used to determine the piston motion through one cycle. For the shortest possible waveform and the chosen thruster design parameters, the model predicted the piston to reach its maximum stroke and then return to its resting position in 47 ms, resulting in a maximum frequency of 21 Hz. Higher frequencies would result in incomplete stroke of the piston during each cycle.

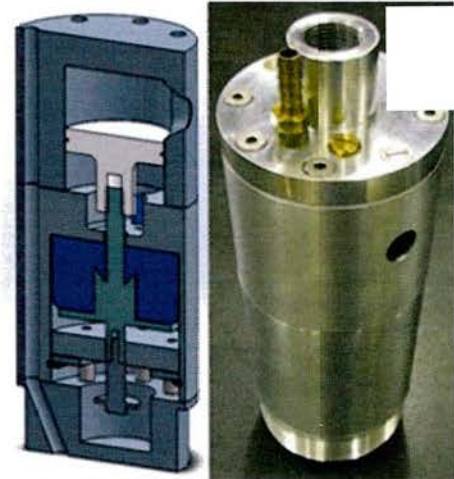


Fig. 2. Model of the thruster (left) and the assembled thruster (right).

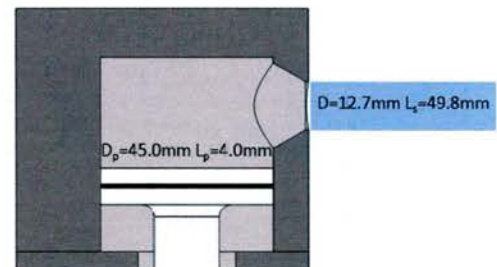


Fig. 3. Dimensions of the cavity and the fluid slug.

## **Force/Moment Measurements**

Two sets of experiments were conducted using a 6-axis load cell to record the forces and moments on the model vehicle. The load cell was an ATI Delta IP68 waterproof transducer located within a flooded box above the water tunnel test section. The model was mounted such that drag force was in the positive x-direction, transverse force in the y-direction, and buoyant force in the z-direction. Since the model was sting mounted below and forward of the load cell, there were also moments produced by the operation of ZNMF thruster; one about the z-axis with a 10.53 inch moment arm; and one about the x-axis with a 7.00 inch moment arm. Thus, the thruster force was recorded by the y-axis force as well as the x- and z-axes moments.

The first set of experiments was conducted without the use of ventilated cavitation gas, thus making the model fully-wetted. Average forces and moments over four second long runs were recorded for thruster frequencies of  $f=4, 8, 12, 16, 20,$  and  $24$  Hz, with nominal tunnel freestream velocities up to  $U_\infty = 8$  m/s in 1 m/s increments. Four sets of data were collected for each condition.

The second set of experiments included the use of ventilated supercavitation. For this set, the thruster frequency was limited to  $f=16, 20,$  and  $24$  Hz due to constraints on operating time and ventilation gas supplies. Ventilation rates were 50, 100, and 200 slpm and nominal tunnel freestream velocities ranged from  $U_\infty = 2.0$  to  $8.0$  m/s in 0.5 m/s increments. Freestream velocities for particular ventilation rates were limited by excessive tunnel blockage at impractically low speeds and cavity instability at the higher speeds. Thus, data over the 2.0 to 8.0 m/s velocity range were broken into three overlapping tests, where the 50 SLPM dataset covered the lower speeds, 100 SLPM covered the mid-range speeds, and 200 SLPM covered the higher speeds. As with the fully-wetted data, all samples were time-averaged over four-second intervals. In the ventilated case, however, the runs were repeated six times to account for the observed higher noise in the data.

## **Direct Imaging**

While conducting load cell experiments it was observed that cavitation was present in the vicinity of the thruster. This was most readily observable in the core of the ejected vortex rings, but also existed as a secondary structure at higher crossflow velocities. To record the behavior of these cavitation regions, direct imaging of the flow field near the thruster was carried out using a

high-speed video camera over a variety of conditions. All video sequences were recorded at 3,000 frames per second and captured several ingestion/expulsion cycles. For operation in the absence of ventilated supercavitation, video was recorded for  $f = 4, 8, 12, 16, 20$  and  $24$  Hz with  $U_\infty = 0$  to  $6$  m/s in  $1$  m/s increments. Video was also recorded for a limited number of supercavitation cases. For all of the latter cases, thruster frequency was limited to  $f = 20$  Hz. The nominal tunnel freestream velocities were  $U_\infty = 3, 4,$  and  $5$  m/s for  $50$  slpm,  $U_\infty = 4, 5,$  and  $6$  m/s for  $100$  slpm, and  $U_\infty = 5, 6,$  and  $7$  m/s for  $200$  slpm ventilation rates.

### Particle Imaging Velocimetry

Particle Imaging Velocimetry (PIV) was used to examine the velocity field near the vicinity of the thruster in the  $xy$ -plane. The experiments were performed using a LaVision PIV system, which consisted of a double pulse Nd:YAG laser, the associated sheet optics, and a ImagerPro4M 4-megapixel CCD camera. For all tests, a laser sheet was projected into the tunnel from the  $y$ -direction at a level where it bisected the thruster orifice. The laser sheet was setup to cover roughly  $50$  mm upstream and downstream of the orifice. The camera was placed below the tunnel looking upward. In this configuration, the velocity fields captured the toroidal vortices produced by the ZNMF thruster. A schematic of the PIV setup is displayed in Fig. 4.

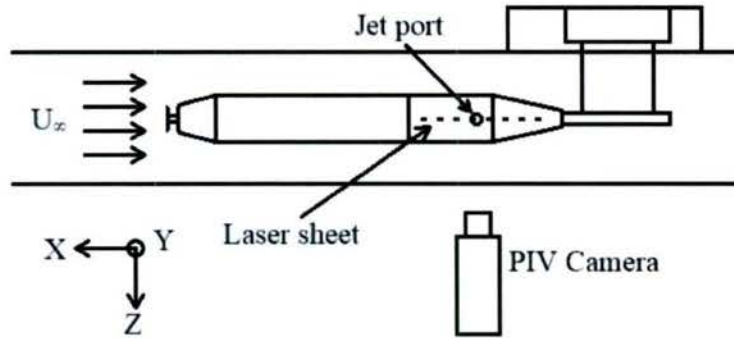


Fig. 4. PIV setup.

The PIV data were collected with the thruster operating at  $f = 20$  Hz, for tunnel freestream velocities up to  $U_\infty = 5$  m/s in  $1$  m/s increments. Data sets were collected over  $16$  phases of the thruster cycle from  $t = 0$  to  $46.88$  ms by  $3.13$  ms increments, with  $t = 0$  corresponding to the instant when power was applied to the solenoid. Fifty instantaneous velocity fields were ensemble-averaged for each set of conditions. An attempt was made to collect PIV data for the

ventilated cases; however, bubbles from the ventilated cavity were entrained in the bulk flow of the tunnel to a degree that the seed particles were covered and large areas of images were affected. For this reason, the PIV data were limited to the fully wetted cases.

### **Uncertainties**

The resolution of the load cell for the loads of interest, force in the y-axis and moments about the x- and z-axes, was  $\pm 1/128$  lbf,  $\pm 3/128$  in-lbf, and  $\pm 1/64$  in-lbf, respectively. To determine the relative force and moment uncertainties, time-averaged values for the thruster operating at  $f = 20$  Hz were used. For the quiescent case with  $U_\infty = 0$  m/s, the uncertainties of the transverse force and x- and z-moments were  $\pm 4.8\%$ ,  $\pm 0.6\%$ , and  $\pm 0.4\%$ , respectively. On the other hand, the uncertainties increased to  $\pm 16.5\%$ ,  $\pm 3.8\%$ , and  $\pm 3.3\%$ , respectively, for the  $U_\infty = 4$  m/s crossflow velocity. The higher uncertainties were primarily due to the reduced thrust at the higher freestream velocity. For the cases with ventilation, the uncertainty of transverse force increased to about 25% while the two moments remained comparable to the fully wetted cases. These values indicate that the two moment measurements have significantly lower relative uncertainties compared to the force measurement.

The uncertainties associated with the PIV data were also calculated based on the error associated with the resolution of pixel displacement. The pixel displacement error associated with the systems used was  $\pm 0.1$  pixels. In the areas of interest, the inter-frame time of PIV acquisition system was adjusted such that pixel displacements were within the suggested range of 2 and 7 pixels, and thus the resulting errors range from 1.4% to 5% for the velocity fields.

## Theoretical Considerations

The primary parameters relevant to the thrust of a ZNMF thruster are the orifice velocity profile  $v(x,z,t)$  during the expulsion phase, the thruster orifice diameter  $D$  and area  $A (= \pi D^2/4)$ , as well as the actuation frequency  $f$  and the expulsion time  $t^*$ . The ejected fluid volume during the expulsion phase  $\mathcal{V}$  can be found by integrating the fluid velocity over the orifice area and the expulsion time.

$$\mathcal{V} = \int_0^{t^*} \int_A v dA dt = V_o A t^* \quad (1)$$

This volume may be written in terms of a characteristic velocity  $V_o$ , which is the averaged velocity over the orifice area  $A$  and the expulsion time  $t^*$ . Given that the ejected fluid volume is known from the piston motion, measurement of  $t^*$  would yield the characteristic velocity  $V_o$ . The stroke ratio may be written in terms of the characteristic velocity,  $L/D = (\mathcal{V}/A)/D = V_o t^*/D$ . As stated in the previous section, the stroke ratio for the setup was fixed at 3.92.

Sample velocity time traces on the centerline of the orifice during the expulsion phase were extracted from the phase-locked PIV data at freestream velocities of  $U_\infty = 0$  and 2 m/s and are shown in Fig. 5. The initiation and termination of the outflow velocity are nearly identical for

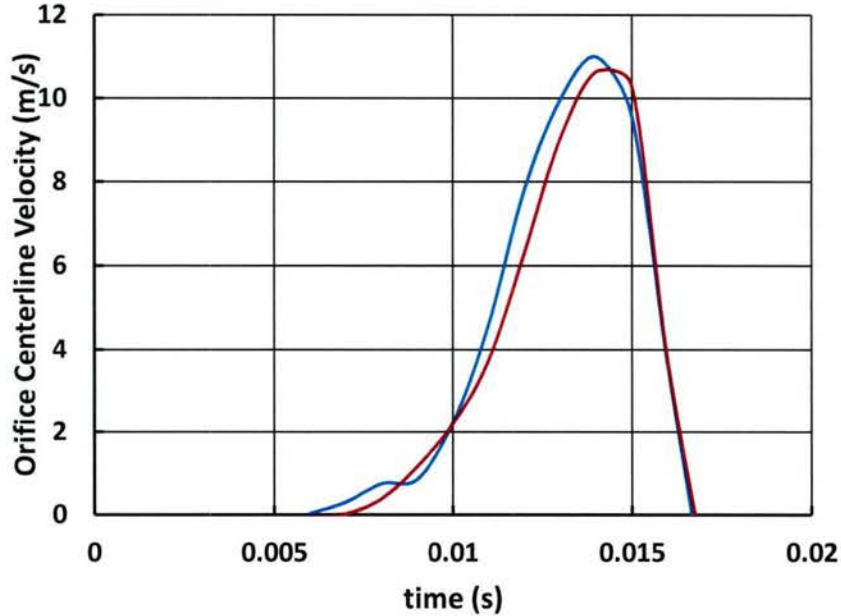


Fig. 5. Velocity time traces at the orifice centerline, blue:  $U_\infty=0$ , red:  $U_\infty=2$  m/s.

the two cases considered. This is not surprising given that the expulsion phase was driven by the impulse of a high-power solenoid operating on a square wave. With this type of forcing one may safely assume a constant  $V_o$  value for all operating frequencies and freestream velocities, as other forces on the piston would be negligible compared to the substantial driving force. The data indicate that the velocity increased to its peak value of about 11 m/s in a time of approximately 8 ms after the motion of piston was initiated. Subsequently, the velocity decreased to zero. Based on these traces, an expulsion time of  $t^* \approx 10$  ms will be used hereafter.

Considering the expulsion time of 10 ms and the known ejected volume and orifice area, a characteristic velocity of  $V_o = 4.98$  m/s is computed using Eq. 1. In the following, all the relevant dimensionless parameters are defined based on this characteristic velocity. The thruster Reynolds number is defined by  $Re = \rho V_o D / \mu$ , Strouhal number by  $St = fD / V_o$ , and the crossflow velocity ratio by  $R = U_\infty / V_o$ . For all cases, the Reynolds number was  $6.3 \times 10^4$ .

To estimate the average thrust, the impulse  $J$  imparted to the fluid slug ejected from the orifice under ideal conditions may be used.

$$J = \int_0^{t^*} \int_A \rho v^2 dA dt = \alpha \rho V_o^2 A t^* \quad (2)$$

Here,  $\alpha$  is used to account for the non-uniform velocity during the expulsion time. If the velocity is uniform across the orifice and throughout the expulsion time,  $\alpha$  would have a value of one. On the other hand,  $\alpha$  would be  $4/3$  for a spatially uniform velocity profile with any triangular variation in time. The time averaged thrust  $\bar{T}$  consists of the slug impulse spread over one cycle period, i.e.

$$\bar{T} = J f = \alpha \rho V_o^2 A t^* f = \alpha \rho V_o A L f \quad (3)$$

The expression in Eq. 3 reveals that the thrust should increase linearly with actuation frequency as long as the pulses are not interacting and the impulse from each expulsion can be accounted for individually in a sequence of repeating cycles. This approach is similar to that used by Kreig & Mohseni (2008); the only difference is that a frequency squared expression was found for the harmonically driven thruster in that setup.

The time averaged thrust may be scaled with the momentum flux of a steady transverse jet with uniform velocity of  $V_o$ . Hence, a steady jet would have a scaled thrust of  $T^* = 1$ , and a

square-wave pulsed jet (without any leading or trailing edge non-uniformities) would have a scaled thrust that is equal to its duty cycle. Scaled thrust may be written as

$$T^* = \frac{\bar{T}}{\rho V_o^2 A} = \frac{\alpha \rho V_o A L f}{\rho V_o^2 A} = \alpha \frac{L}{V_o} f = \alpha \frac{L}{D} St \quad (4)$$

The above expression indicates that scaled thrust is a linear function of the stroke ratio and Strouhal number for the setup. Given that the stroke ratio was fixed at 3.92, the scaled thrust for the thruster used here should be

$$T^* = \alpha(3.92)St . \quad (5)$$

For an impulsive velocity profile during the expulsion phase, it is expected that  $\alpha$  would be greater than one, and as much as 4/3 for a trapezoidal velocity profile. The parameter  $\alpha$  can be computed by integration of the velocity profile across the orifice plane during the expulsion time.

## Results

The time averaged thrust along with direct flow visualization and velocity and vorticity fields from PIV are presented in this section. The data are categorized for the quiescent, fully wetted crossflow, and ventilated cavity cases below.

### Quiescent Case

In the absence of crossflow, the time averaged thrust obtained through three different measures is plotted as a function of frequency. The data in Fig. 6 are presented in engineering units for a sense of scale. Thrust derived from the two moment coefficients (pitch and roll moments divided by their respective moment arm) were nearly identical for the entire frequency range, and these values were greater than the directly measured transverse force. Given that the force derived from the moments had the least uncertainty, the roll moment about the x-axis  $M_x$  was chosen as the best indicator of thrust created by the thruster. This derived thrust measurement is used in all subsequent plots.

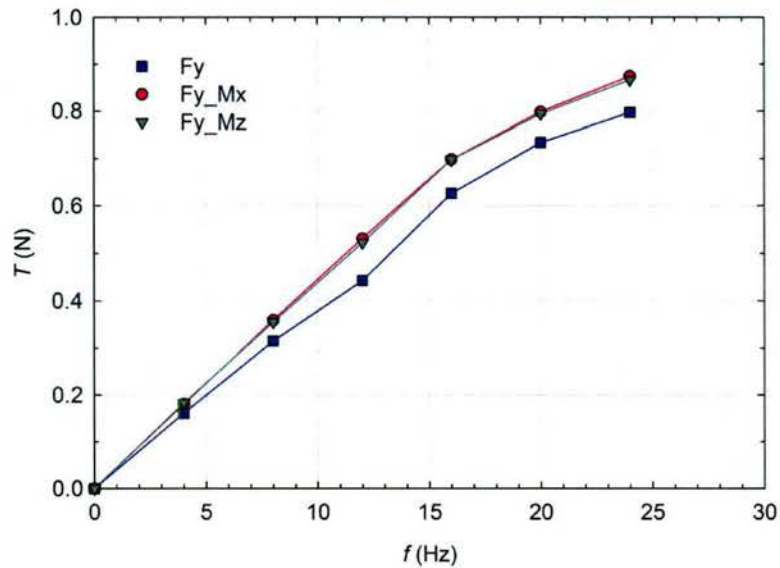


Fig. 6. Measured thrust as a function of actuation frequency.

Scaled thrust  $T^*$  in the absence of crossflow is plotted against the Strouhal number in Fig. 7. The Strouhal numbers correspond to the frequencies in Fig. 6. The maximum scaled thrust for the highest Strouhal number was 0.28. In agreement with the model presented in the previous section, scaled thrust increased linearly with Strouhal number up to  $St = 0.04$ . At greater Strouhal numbers, scaled thrust increased but not at the same rate. This is due to the solenoid

response time which limited the actuation frequency to  $\sim 21$  Hz. Larger frequencies result in the actuation of the solenoid prior to the piston reaching its resting position. Even though not presented, scaled thrust continued to increase slightly for even greater frequencies than those shown in Fig. 7; however, thrust decreased eventually at frequencies beyond 30 Hz.

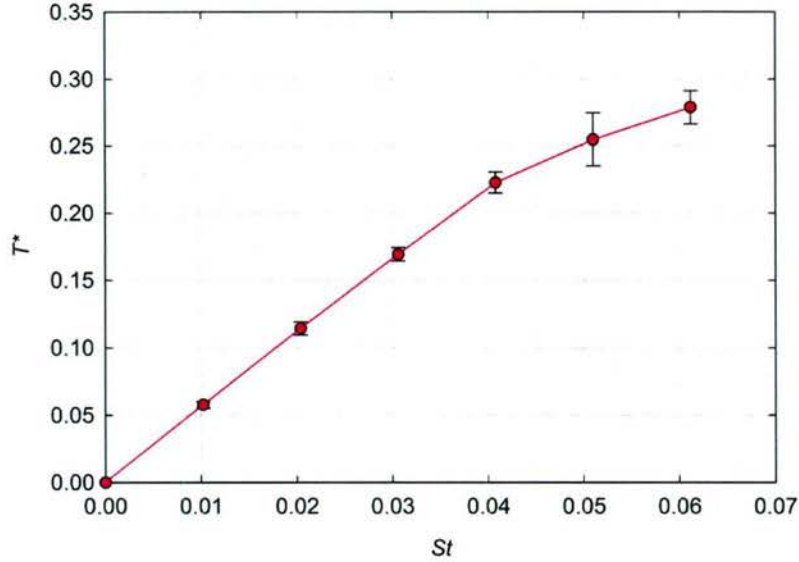


Fig. 7. Scaled thrust as a function of Strouhal number.

The data in Fig. 7 have a slope of  $d(T^*)/d(St) = 5.51$  for  $St \leq 0.04$ . This can be compared against the theoretical expression from the model that predicted a slope of  $\alpha(L/D) = 3.92\alpha$ . Assuming a value of  $\alpha = 4/3$  for a trapezoidal orifice velocity time history, the measured thrust is only 5% greater than the theoretical model. The close correspondence between the theoretical model and the measured thrust verifies the approach pursued in the previous section.

A composite image of the cavitating core of a vortex ring produced by the thruster operating at a frequency of  $f = 4$  Hz corresponding to Strouhal number of  $St = 0.010$  is shown in Fig. 8. This image revealed the nearly constant celerity of the ring structure as it convected away from the orifice at approximately 3.25 m/s. Direct imaging also captured the transition of the ring structure from laminar (at approximately one diameter) to turbulent state (at approximately four diameters). Turbulence was indicated by the emergence of irregularities at  $\sim 15$  ms in Fig. 8. Direct imaging at various operating frequencies revealed very similar vortex core behavior, supporting thrust measurements that suggest the behavior of individual pulses are independent of Strouhal number within the linear regime.

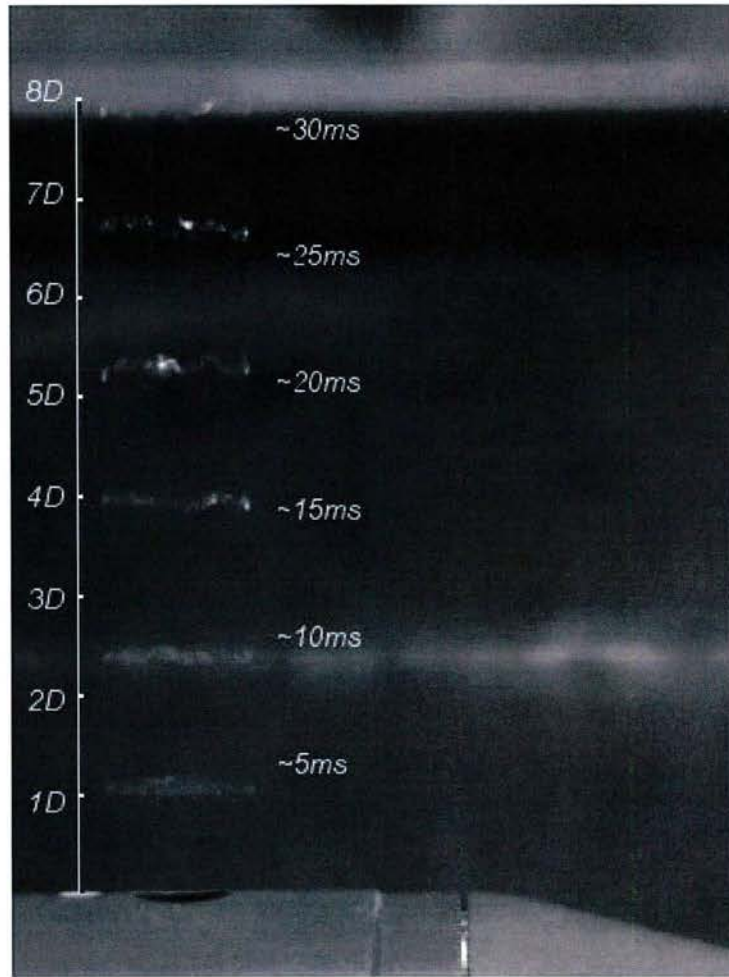


Fig. 8. Composite image of the cavitating vortex core at 6 instants.

The ensemble-averaged PIV velocity fields for 16 phases are shown in Fig. 9. Despite the fact that the rising edge of the square wave began at  $\phi=0$  and the falling edge started just before  $\phi=4$ , the expulsion of fluid from the thruster occurred mostly in phases  $\phi=4$ , 5, and 6. This is likely the result of inductance of the solenoid coil, causing it to operate out of phase; this phase delay is expected to be consistent among all phase-locked PIV data. The effective start of a cycle can be assumed to occur between  $\phi=3$  and  $\phi=4$ .

In addition to the expulsion phase occurring in a different instant than one might naturally expect, the ingestion of fluid back into the synthetic jet chamber began immediately after the expulsion phase but continued through  $\phi=15$  and wrapped to the beginning, ending finally at  $\phi=3$  (just before the cycle repeated). The unsteady nature of the ingestion phase should also be noted. Fluid appeared to be drawn back with the greatest velocity at  $\phi=15$ , but virtually ceased at  $\phi=0$ , only to be drawn in again at  $\phi=1$ .

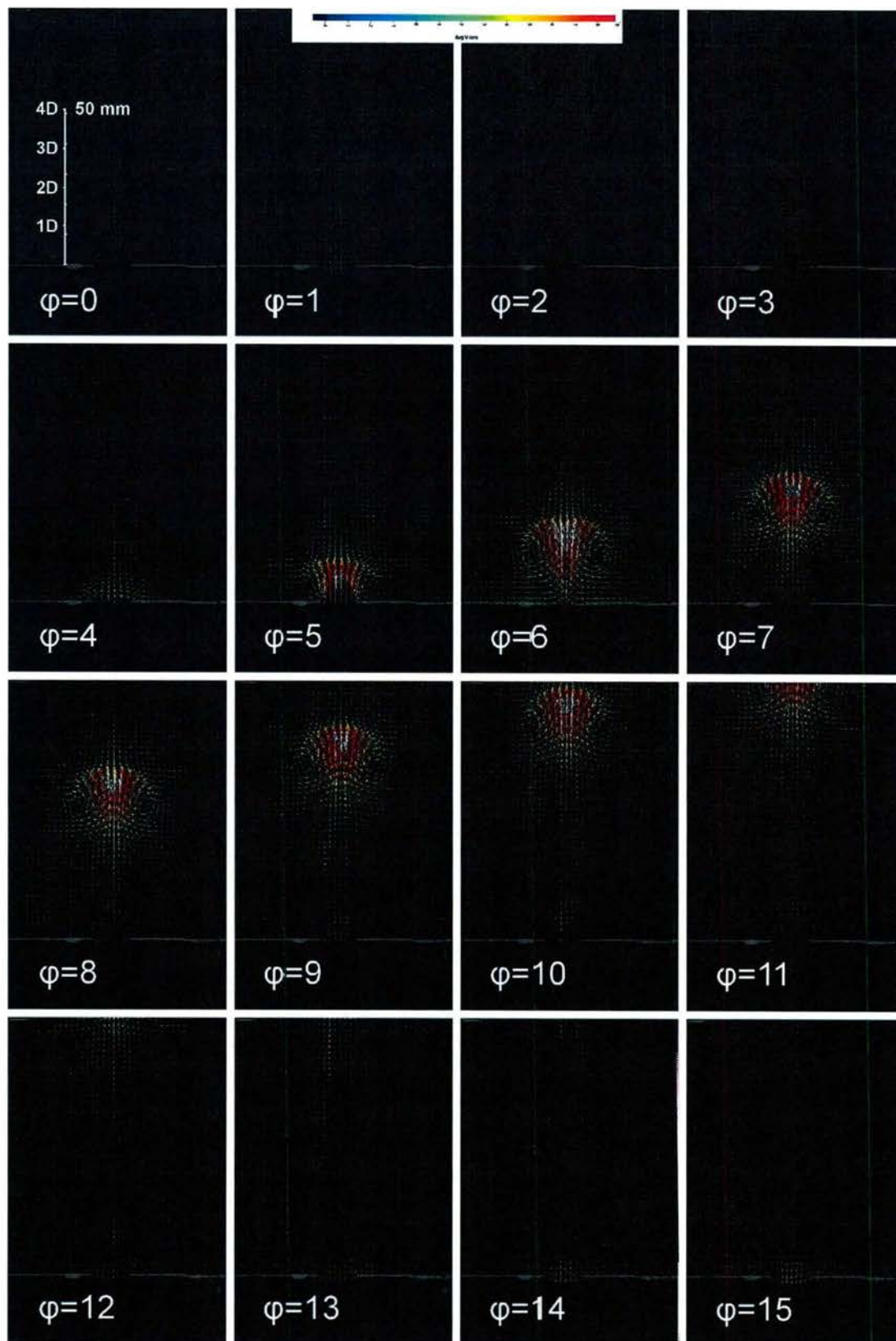


Fig. 9. Phase-locked PIV velocity fields (16 phases) in quiescent media.

The vorticity fields obtained from the ensemble-averaged velocity field data in quiescent media are presented in Fig. 10. From  $\varphi=0$  the continued ingestion from the previous cycle is seen. The wake of the previous ring is barely visible above two small counter-rotating structures of fluid being drawn back into the orifice. These weak regions of vorticity associated with ingestion continued through  $\varphi=3$ . At  $\varphi=4$ , the expulsion of fluid began with an intense reversal of vorticity in these regions. The vorticity increased drastically through  $\varphi=5$  and the resulting ring continued to convect at  $\varphi=6$ . At this point, peak vorticity of  $\sim 2000 \text{ s}^{-1}$  can be observed in the core of the ring. From  $\varphi=7$  to  $\varphi=11$ , the ring structure moved out of the field of view with a relatively constant celerity, leaving behind a wake of like vorticity. From  $\varphi=12$  to the conclusion of the cycle, the ingestion of fluid by vorticity with opposite sign of the ring structure can be seen. The ingestion vorticity peaked at  $\varphi=15$ , but continued and wrapped to the start of the following cycle though  $\varphi=3$ .

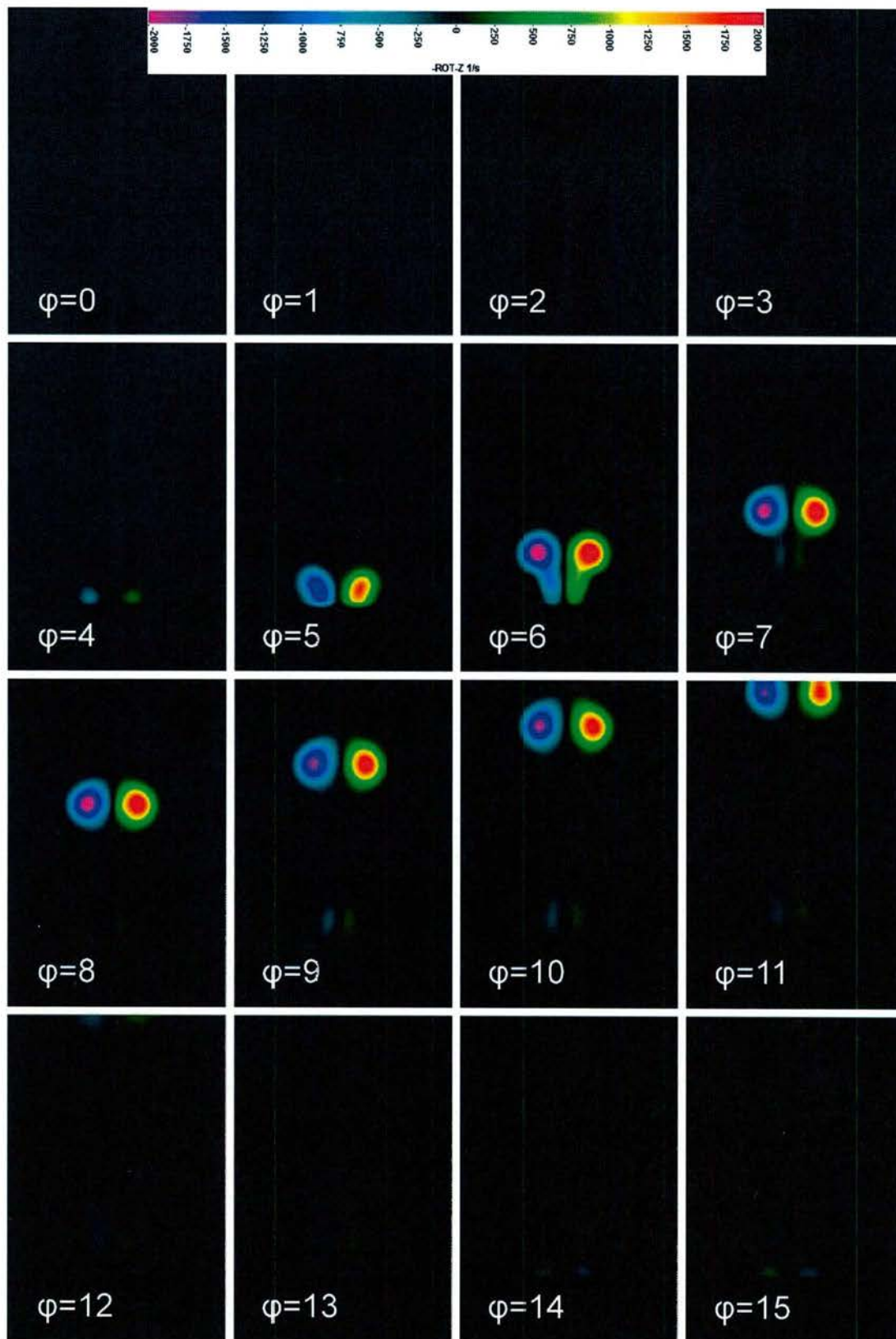


Fig. 10. Vorticity fields (16 phases) from phase-locked velocity data in quiescent media.

## Crossflow Case

The dependence of scaled thrust on Strouhal number is plotted in Figs. 11 and 12 for crossflow velocity ratios  $R = 0$  to 1.25. The solid line in these plots represents the quiescent case  $R = 0$ . The data have been separated into low crossflow velocity ratio  $R$  (Fig. 11) and high  $R$  (Fig. 12) cases roughly according to the past studies of steady and pulsed jets where a transition at the crossflow velocity ratio of about  $R \approx 0.5$  has been reported. For all crossflow velocity

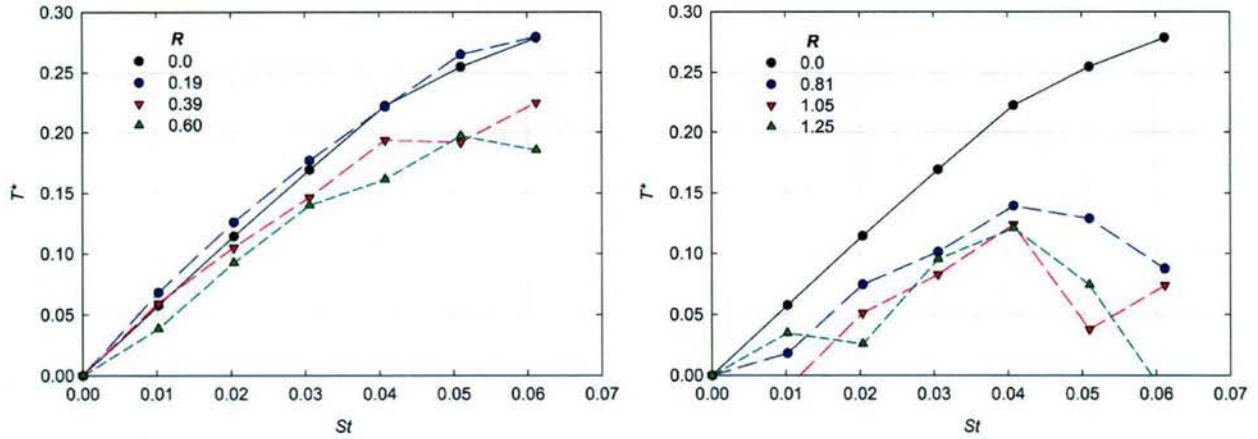


Fig. 11. Scaled thrust for low crossflow velocities. Fig. 12. Scaled thrust for high crossflow velocities.

ratios, a linear relationship can be observed between scaled thrust and Strouhal number up to a critical point, beyond which the scaled thrust does not increase as rapidly. The data indicate that the slope  $d(T^*)/d(St)$  in the linear regime generally decreases as crossflow velocity ratio increases. It is clear from Fig. 11 that the linear regime extends to a Strouhal number of  $St = 0.041$  and thrust continues to increase at higher frequencies for the low crossflow velocity ratios. On the other hand, thrust decreases for Strouhal numbers greater than 0.04 for the high crossflow velocity ratios. This is particularly true for true for the  $R = 1.25$  case in Fig. 12.

To further explore the effects of crossflow velocity, the same scaled thrust data are plotted against the crossflow velocity ratio for each frequency in Fig. 13. As expected, higher Strouhal numbers generally result in higher scaled thrust values. Also, it is observed that scaled thrust drops off sharply as the crossflow ratios increases towards one. Furthermore, the data suggest that for Strouhal numbers up to  $St = 0.04$ , scaled thrust decreases linearly with the crossflow velocity.

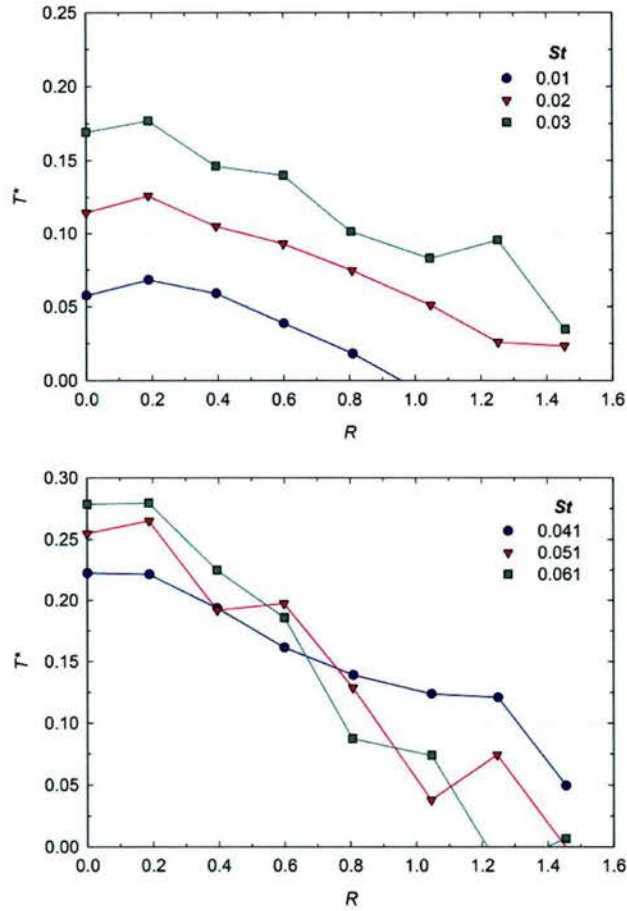


Fig. 13. Scaled thrust as a function of crossflow velocity ratio.

To examine this aspect, the slope  $d(T^*)/d(St)$  in the linear Strouhal number regime for each crossflow velocity ratio was computed and plotted against  $R$  in Fig. 14. Again, a linear relationship with crossflow velocity ratio is observed. The data in Figs. 11 – 13 indicate that scaled thrust increases linearly with actuation frequency, up to the solenoid limit, and decreases linearly with the crossflow velocity. Thrust is greatly reduced for crossflow velocities greater than one.

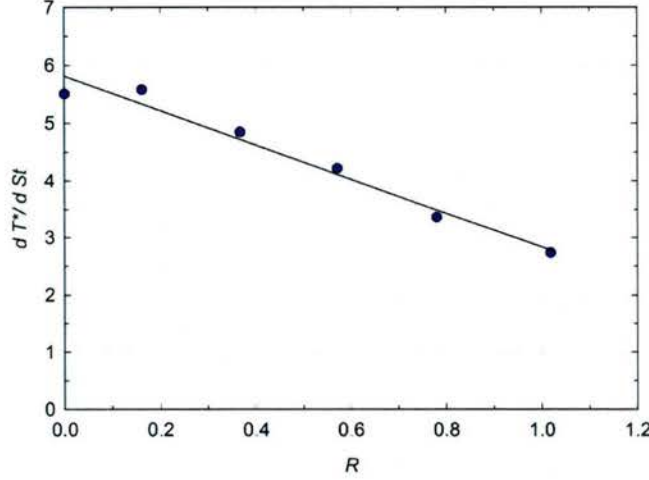


Fig. 14. Slope of scaled thrust as a function of crossflow velocity ratio.

A linear regression of the data in Fig. 14 yields the expression in Eq. (6). The linear fit

$$\frac{dT^*}{dSt} = 5.81 - 2.98 \frac{U_\infty}{V_o} \quad (6)$$

results in a peak scaled thrust of  $5.81 St$  under quiescent conditions. This is approximately 5% greater than the  $5.51 St$  found directly in the quiescent case. It also implies that the ZNMF thruster produces no transverse thrust at a velocity ratio of 1.94. Rewriting the above expression in terms of the operating parameters for this thruster provides an expression for the dependence of the time averaged thrust on the frequency, orifice diameter, and crossflow velocity.

$$\frac{\bar{T}}{\rho V_o^2 A} = \left( 5.81 - 2.98 \frac{U_\infty}{V_o} \right) \frac{f D}{V_o} \quad (7)$$

A composite image similar to the quiescent case in Fig. 8 is presented in Fig. 15 where the thruster was operating in a 1 m/s crossflow, corresponding to  $R = 0.19$ . In this figure, a cavitating vortex ring can be observed having a velocity comparable to the quiescent case in the near field, though it appeared to be in a transitional state by the time it reached one orifice diameter from the hull. As the vortex core passed two jet diameters at 10 ms, its structure appeared mostly unchanged from that at 5 ms; however, it had washed slightly downstream due to the presence of crossflow. At the 15 ms timestamp, the ring structure was bent and turned into the direction of crossflow. At this point, the ring appeared turbulent and unstable. At 20 ms, the ring was breaking up. In videos, the fluid circulation was still evident, but there was no longer a

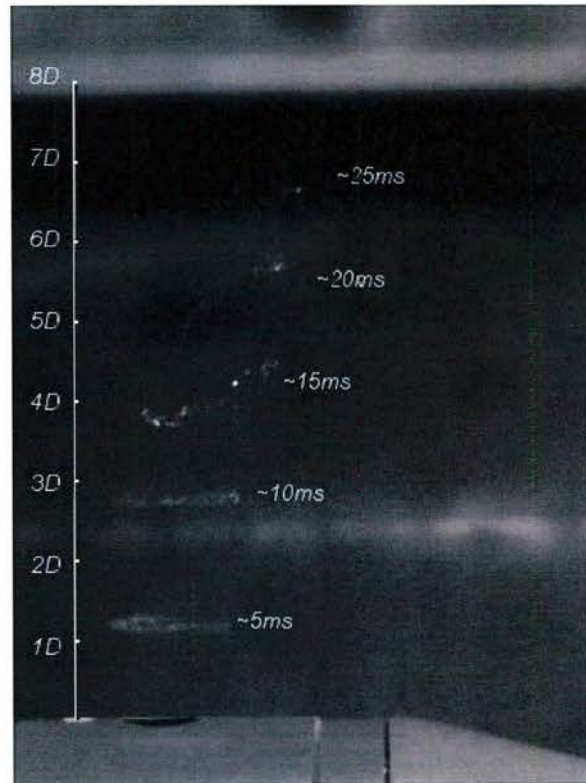


Fig. 15. Composite image of cavitating vortex ring core at  $U_\infty = 1$  m/s,  $R = 0.19$ .

continuous ring structure. By the final timestamp, only a few cavitation bubbles remained as the structure broke down and washed downstream. A similar progression was observed for the 2 m/s crossflow velocity ( $R = 0.39$ ), except that break down of the vortex core was hastened.

A composite image for the 3 m/s crossflow velocity ( $R = 0.60$ ) is shown in Fig. 16. In this image, the leading and trailing edges of the cavitating ring structure convected more quickly than the near and far edges. As this occurred, the vortex ring structure quickly folded. By  $\sim 5$  ms the cavitating core has already bowed significantly inward. Additionally, a small amount of cavitation occurring in the normal direction between the orifice and cavitating ring can be observed in Fig. 16. By the following timestamp, this cavitation region had collapsed. In most cases, this collapse disrupted the ring structure, causing it to break up before reaching two orifice diameters from the hull.

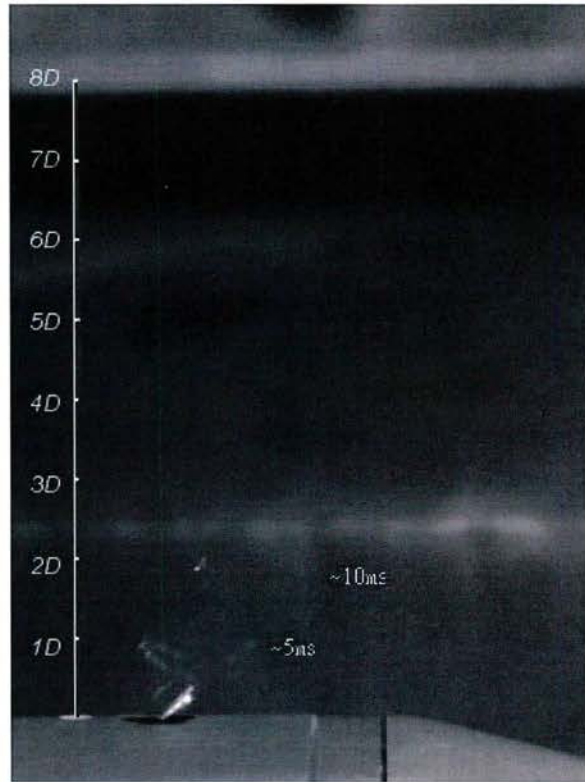


Fig. 16. Composite image of cavitating vortex ring core at  $\bar{U}_\infty = 3$  m/s,  $R = 0.60$ .

For greater crossflow velocity ratios,  $R > 0.6$ , the evolution and breakup of structures occurred very close to the orifice and over very short periods of time. For this reason, composite images were not feasible, as images from different timestamps would be overlapped and difficult to distinguish from one another. Instead the evolution of the cavitating vortex ring is depicted for the larger crossflow velocity ratio cases. Direct imaging of the flow emerging from the orifice for the 4 m/s crossflow velocity ( $R = 0.81$ ) is shown in Fig. 17. In this sequence, the additional cavitation region described for the  $R = 0.60$  case was more prominent. Less cavitation within the vortex core itself, and much earlier and more significant cavitation in additional strands can be seen in Fig. 17. This phenomenon was visible when the ring was as close as one-half orifice diameter from the hull. The folding of the vortex ring and collapse of the transverse cavitation contributed to the breakup of the vortex ring within the first 1.5 diameters of the hull.

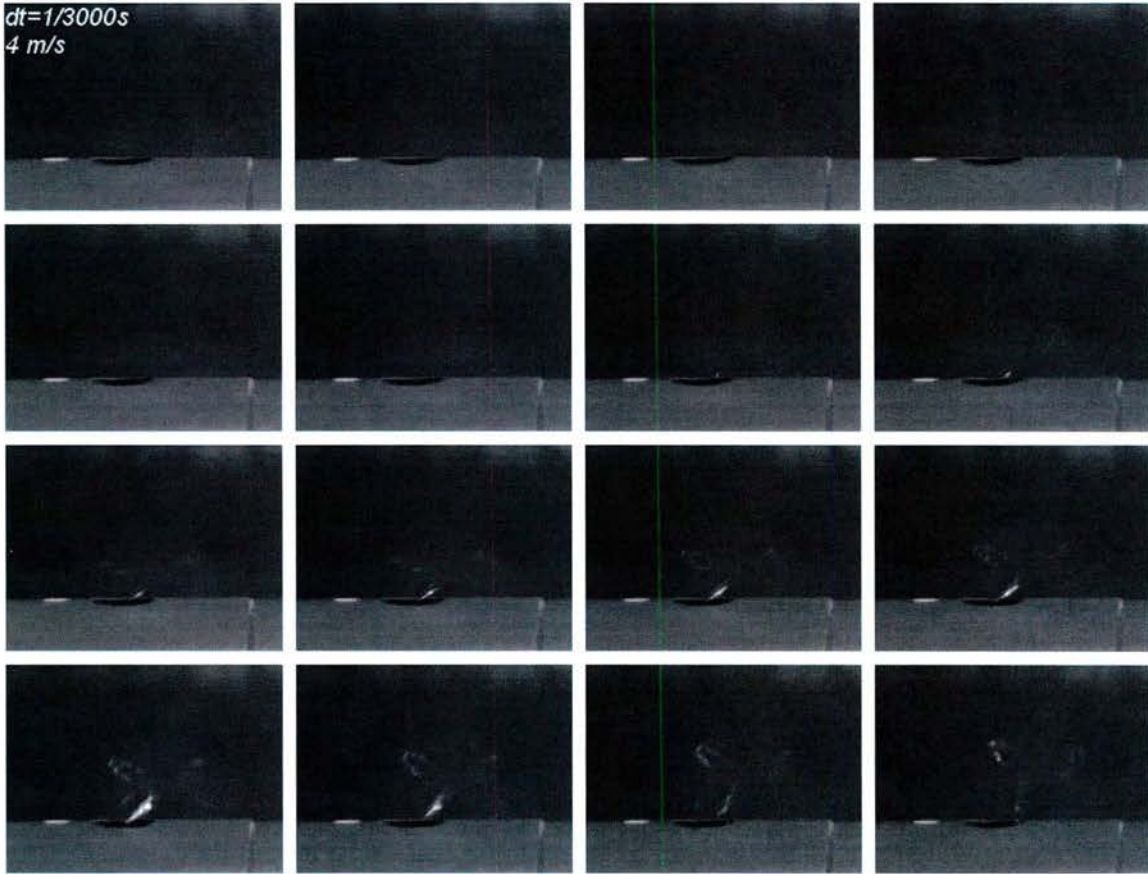


Fig. 17. Evolution of the vortex core for  $U_\infty = 4$  m/s,  $R = 0.81$ .

The evolution of the cavitating flow field including the vortex core at  $U_\infty = 5$  m/s, corresponding to  $R = 1.05$  is presented in Fig. 18. This image set is extended to show an emerging behavior in the ingestion phase of operation at this crossflow velocity ratio. In keeping with the trend seen in the lower crossflow velocity ratio cases, the additional cavitation stands became more pronounced while the ring cavitation became fainter. A weak ring became visible only as the additional cavitation stands began to collapse, and the ring quickly broke down. Once the additional cavitation stands had completely dissipated, only a chaotic churning structure that was no longer a ring can be seen. As this churning continued, a new region of cavitation appeared at the orifice.

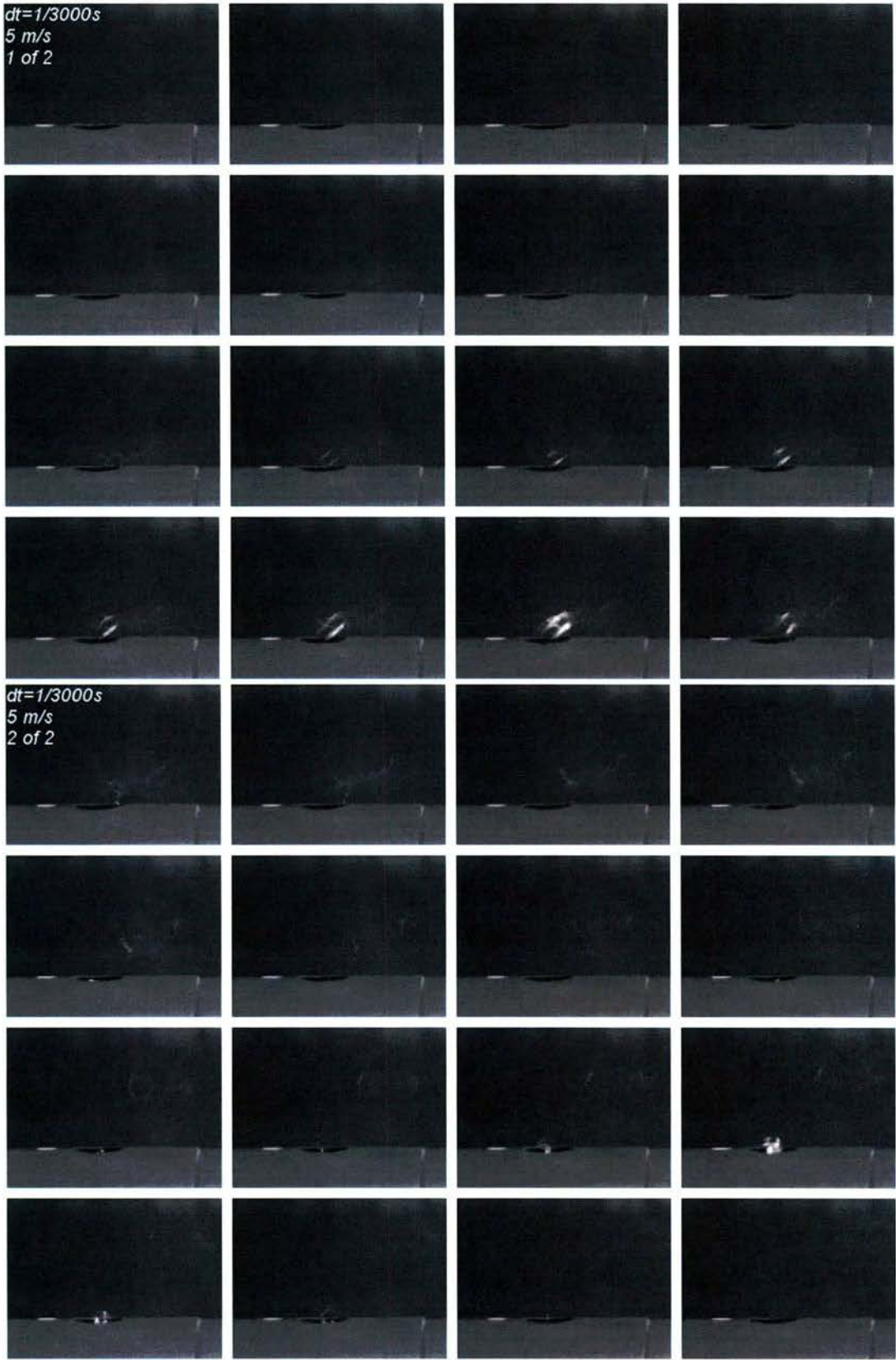


Fig. 18. Evolution of the vortex core for  $U_\infty = 5\text{ m/s}$ ,  $R = 1.05$ .

The evolution of velocity field within the first five orifice diameters for the  $R = 0.19$  case is shown in Fig. 19. The data revealed behavior consistent with the quiescent case in Fig. 9. The formation and evolution of the vortex structure occurred during the same phases as the quiescent case and the vortex core convected at the same celerity. The one exception was that peak ingestion velocity appeared to occur at  $\varphi=0$  rather than  $\varphi=15$ . Otherwise, the only observable change was the slight downstream motion of the vortex structure.

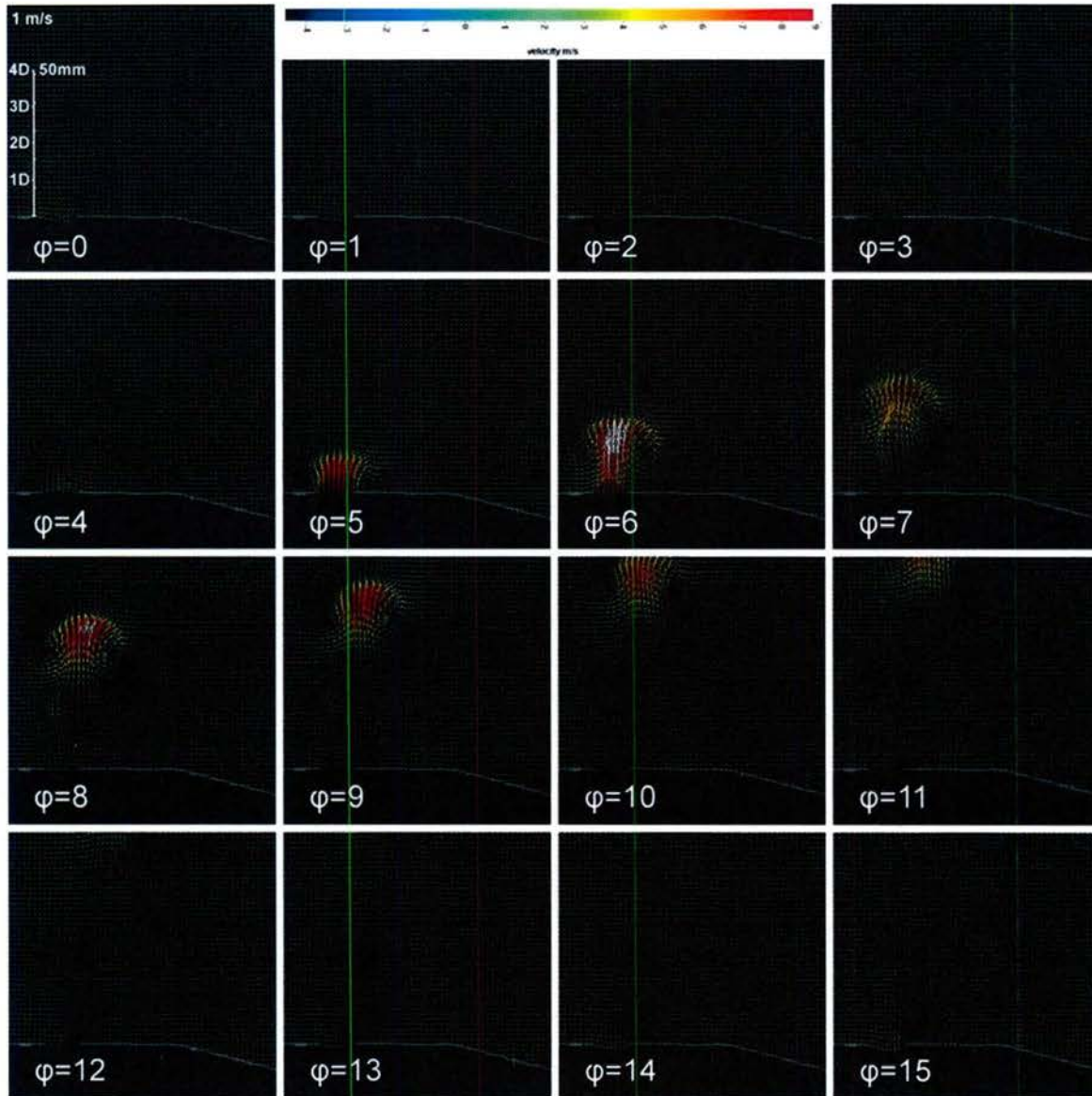


Fig. 19. Velocity field evolution for  $R = 0.19$ .

For the  $R = 0.39$  case in Fig. 20, flow field behavior began to change. The vortex structure no longer vacated the field of view by  $\varphi=11$ . Instead, the structure broke down and was washed away along the top of the field of view. The expulsion phase began at  $\varphi=4$  and ended by  $\varphi=6$ . Although the thruster was operated at the same frequency and duty cycle as other cases, the ingestion phase seems to be delayed slightly with respect to the quiescent case, with no fluid flowing into the orifice until  $\varphi=12$ . The ingestion phase then appeared to achieve its peak velocities from  $\varphi=15$  to  $\varphi=1$ . As in the quiescent case, no secondary ingestion was visible.

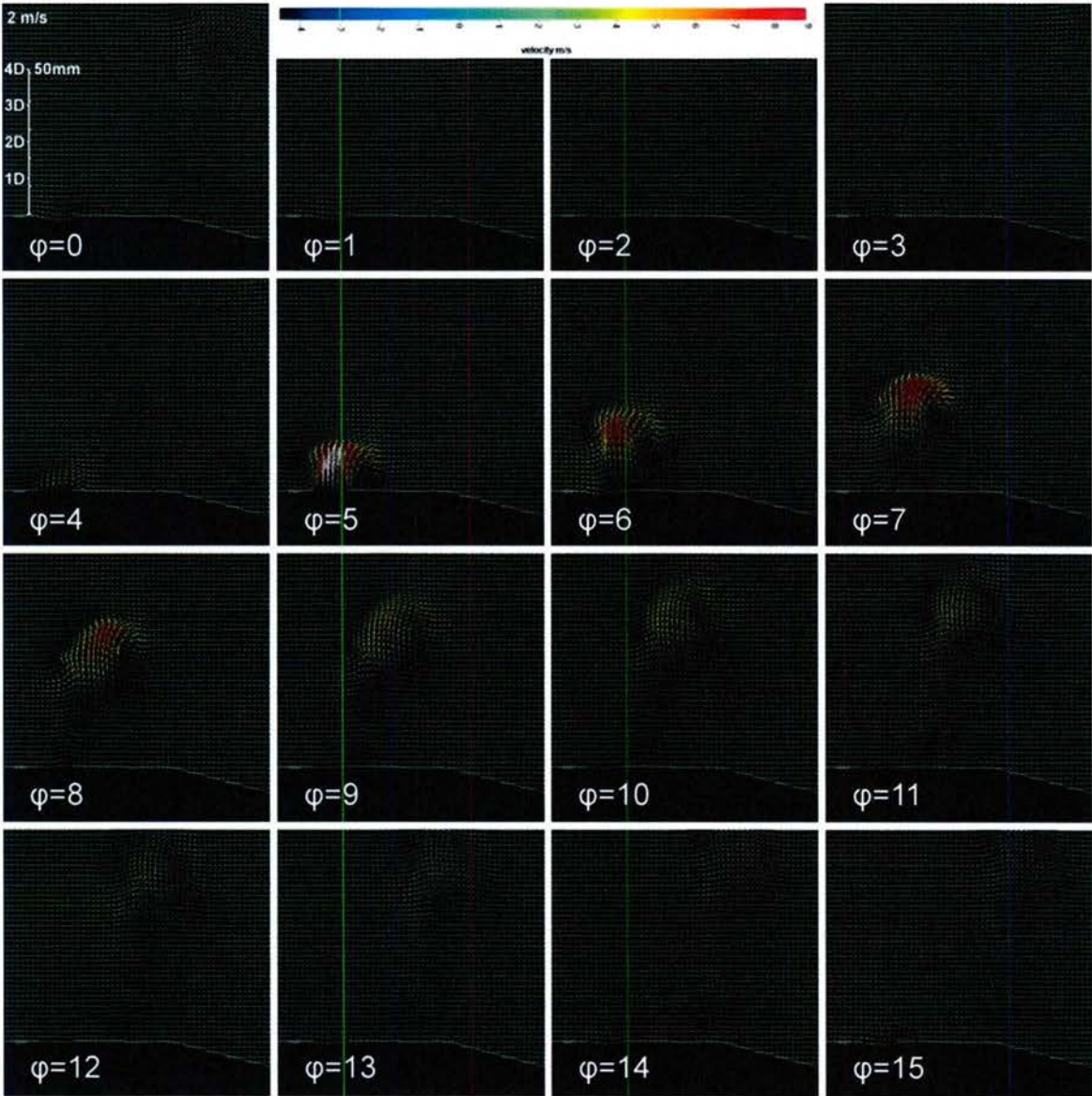


Fig. 20. Velocity field for  $R = 0.39$ .

The velocity field for the  $R = 0.60$  case in Fig. 21 displays very similar behavior to the  $R = 0.39$  case. The one noteworthy difference between the two cases is that the vortex structure appeared to break up sooner and was washed out of the field of view downstream without having traveled as far from the hull. The breakup was best captured in  $\varphi=7$  and  $\varphi=8$ , where the downstream edge of the vortex ring was traveling significantly faster than the upstream edge.

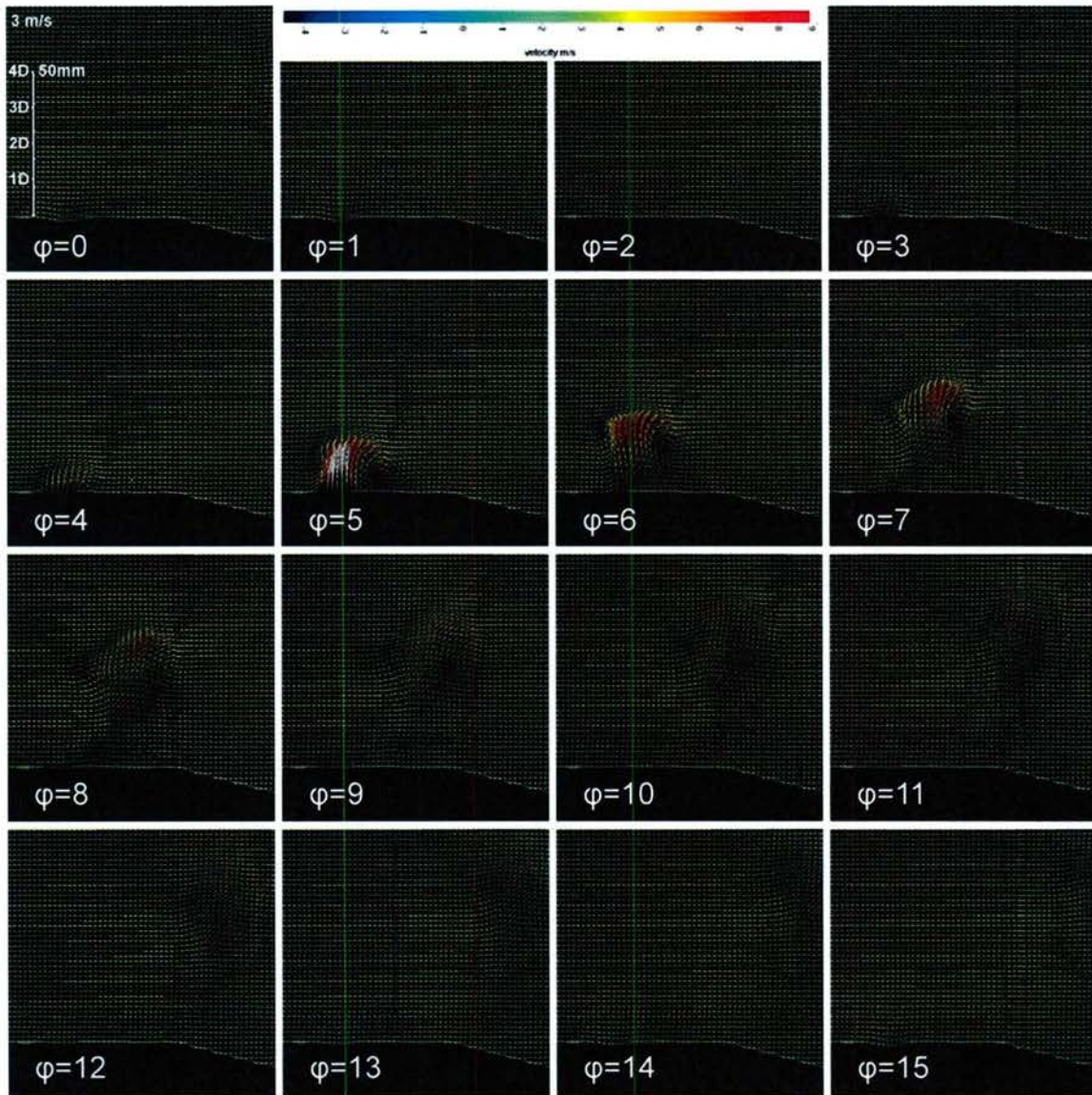


Fig. 21. Velocity field at  $R = 0.60$ .

The  $R = 0.81$  case is presented in Fig. 22. Recalling that direct video imaging revealed very pronounced cavitation at this crossflow velocity ratio, a similar trend is difficult to decipher in the velocity field. The expulsion and ingestion phases continued to be consistent with the other

$R$  value cases. The ring breakup, however, happened even earlier. In  $\varphi=5$  and  $\varphi=6$  phases, the upstream and downstream sides of the vortex structure appeared to develop differently. In  $\varphi=7$  phase, a region which was chaotic and amorphous emerged, and washed out of the field of view by  $\varphi=12$  phase.

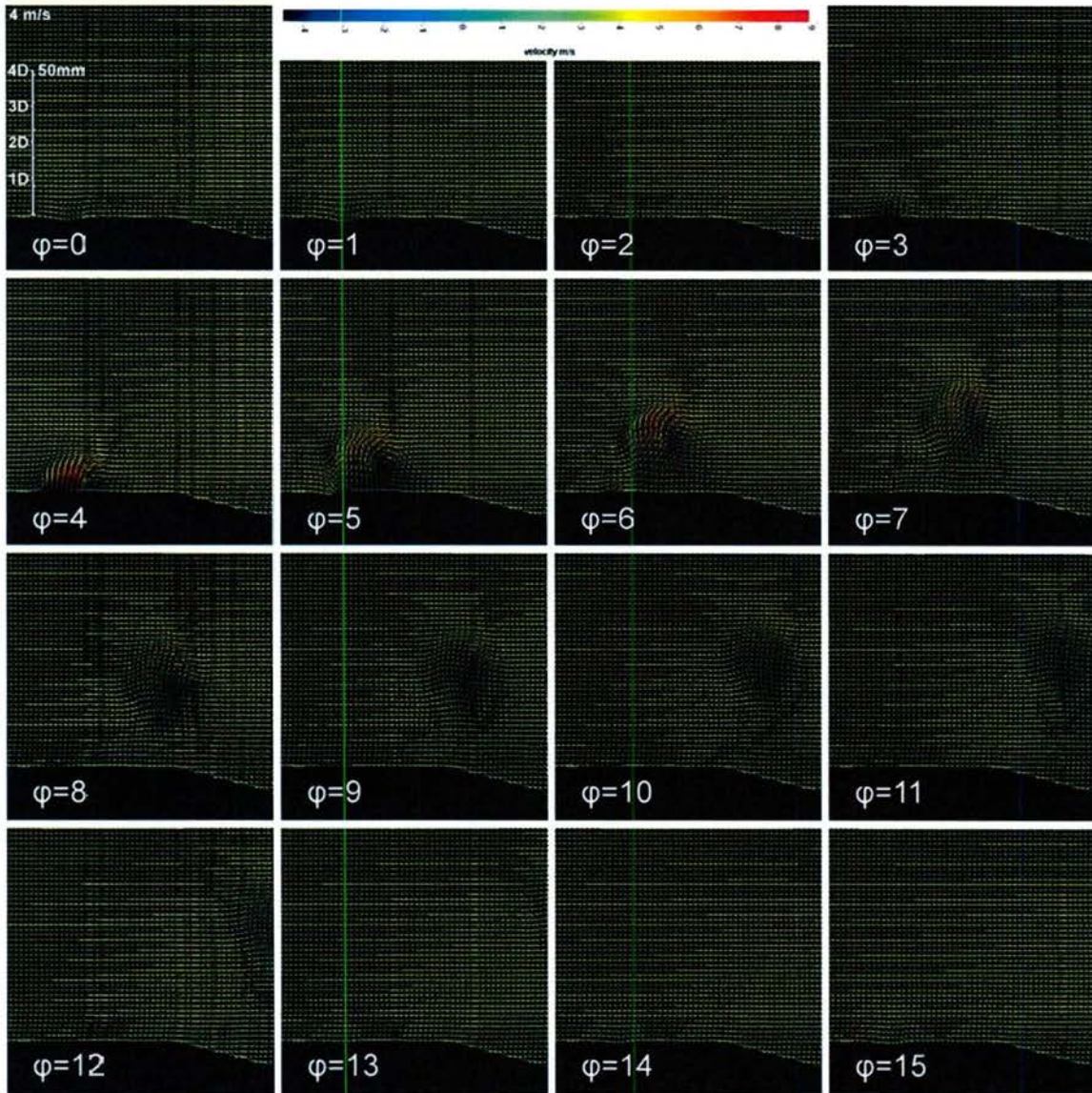


Fig. 22. Velocity field at  $R = 0.81$ .

The highest crossflow velocity field corresponding to  $R = 1.05$  is presented in Fig. 23. In the  $\varphi=1, 2$  and  $3$  phases, where one would expect to see the end of the ingestion phase, we instead observe that the inward component of velocity was dwarfed by the strong  $U_\infty = 5$  m/s crossflow. In  $\varphi=4$  phase, where the first indication of the outstroke occurred, a velocity profile

near the orifice that was similar to that of moderate crossflows was present. However, by  $\varphi=5$  a new behavior emerged; there appeared to be a cessation of bulk outward flow. In fact, at the upstream end of the orifice, fluid was rushing inward. It is unclear from the velocity field data whether this was an accurately recorded field, or the result of the processing software's inability to cross-correlate the image pairs due to increased cavitation near the orifice.

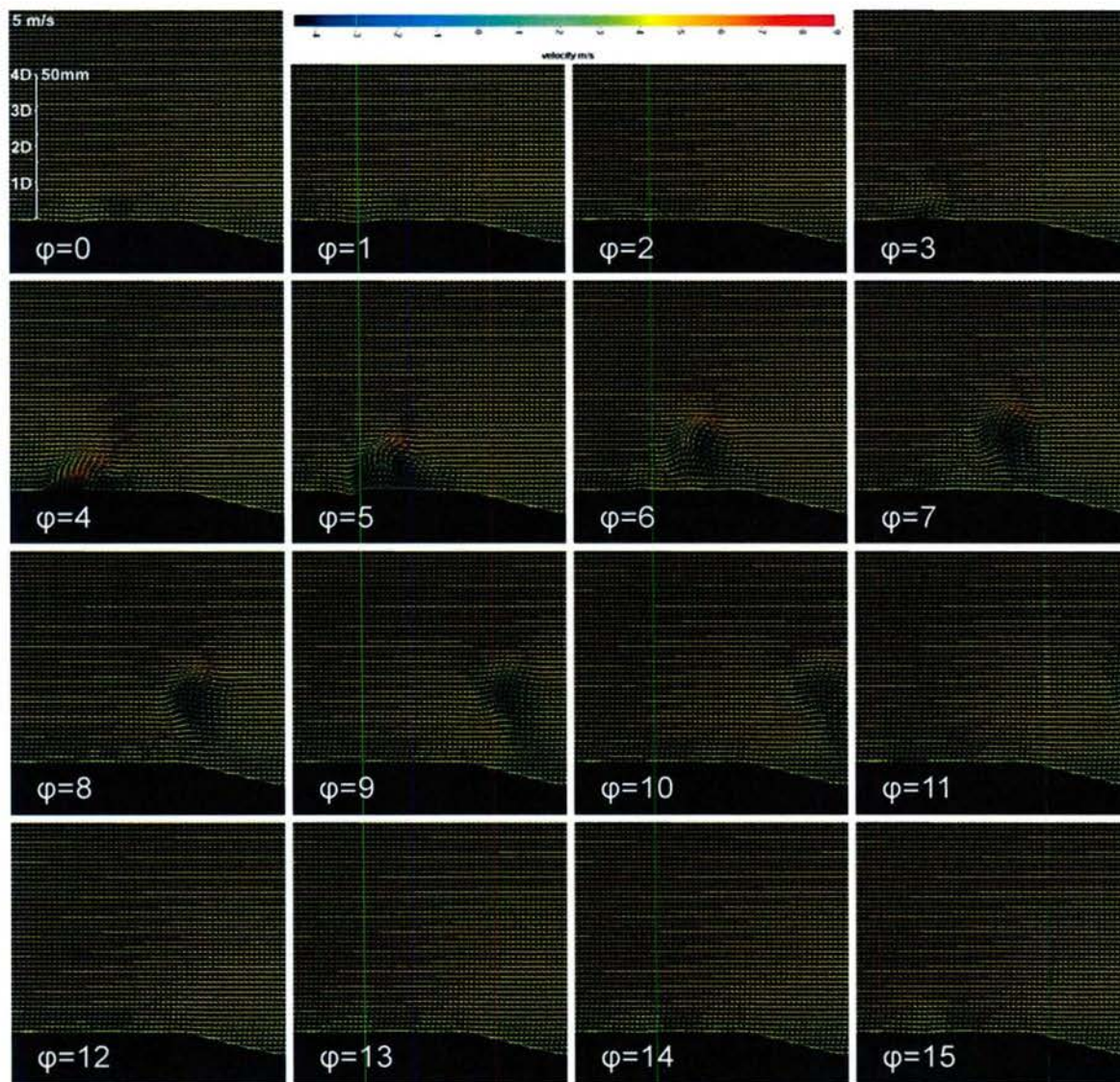


Fig. 23. Velocity field at  $R = 1.05$ .

Vorticity fields were computed from the phase-locked velocity fields for crossflow cases up to  $R = 1.05$ . The evolution of the vorticity for the  $R = 0.19$  is shown in Fig. 24. The outstroke phase began at  $\varphi=4$ , with negative vorticity on the upstream edge of the orifice and positive

vorticity on the downstream edge, and vorticity increased in these regions through  $\varphi=5$ . In  $\varphi=6$  phase, the vortex structure had propagated approximately one diameter away from the hull. At this point, vorticity at the core of the ring was near its maximum of  $\pm 2000 \text{ s}^{-1}$  and two trailing regions of moderate vorticity could be observed. In  $\varphi=7$ , the ring had disconnected from the feeding shear layer, and the trailing vorticity had separated into a secondary structure. At this crossflow velocity ratio, the vortex ring was a stable structure which had slightly pitched in the direction of crossflow. The ring left the field of view by  $\varphi=11$ .

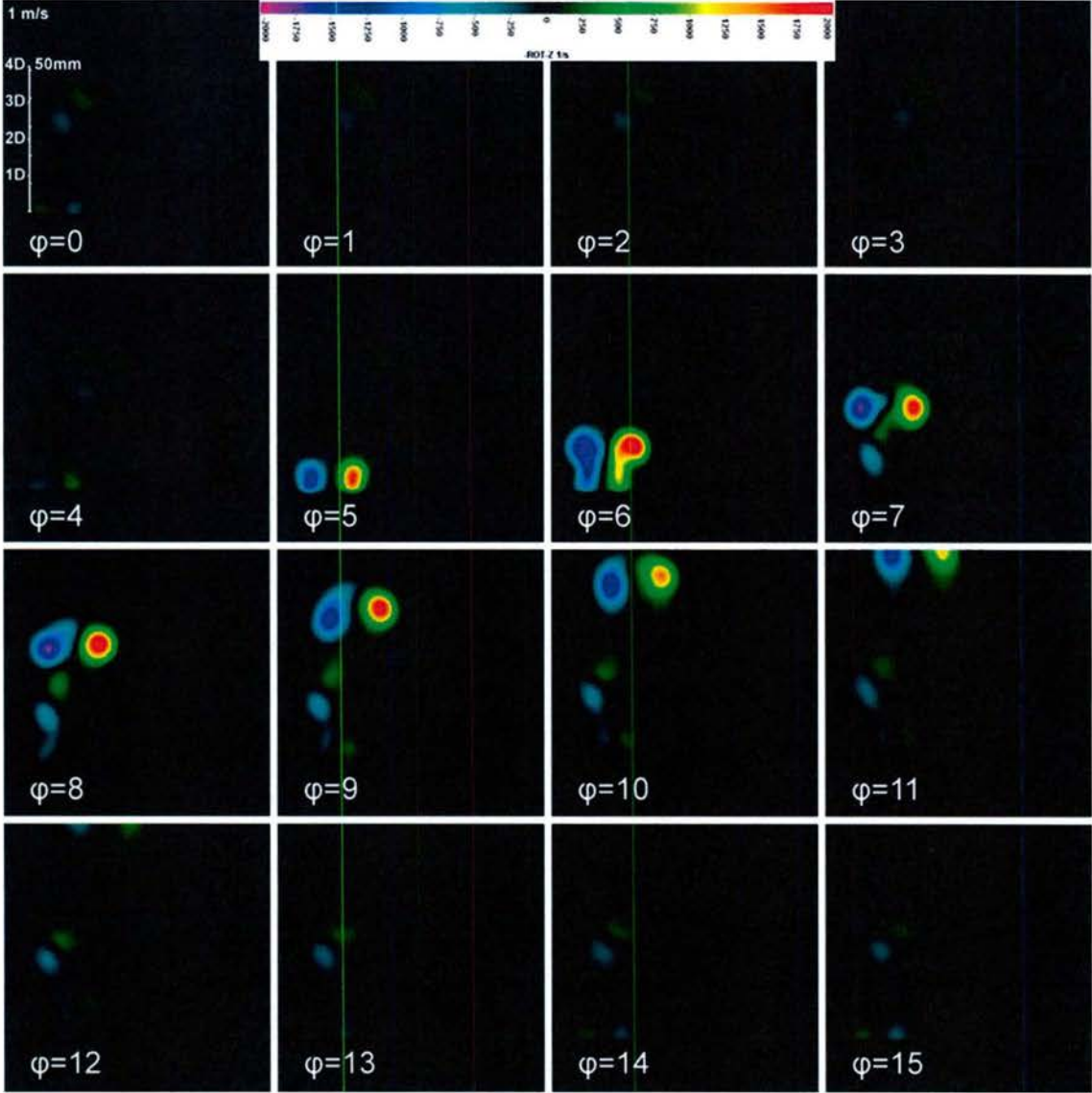


Fig. 24. Evolution of the vorticity field at  $R = 0.19$ .

In Fig. 24, the ingestion phase began in  $\varphi=11$ , where positive vorticity appeared near the leading edge of the orifice. The ingestion phase continued through  $\varphi=15$  and wrapped to the beginning, finally ending in  $\varphi=2$ . The peak vorticity near the orifice during the ingestion phase was at  $\varphi=15$ . During the ingestion phase, the secondary structure described above continued to linger 2 to 4 orifice diameters from the hull. This secondary structure translated downstream very slowly and decreased in vorticity, but was ultimately disrupted by the subsequent expulsion.

The vorticity field for the  $R = 0.39$  case is shown in Fig. 25. As with the  $R = 0.19$  case, initial negative vorticity appeared on the upstream edge of the orifice and it increased through  $\varphi=5$  where the core vorticity on the upstream side of the vortex ring was approximately  $1800 \text{ s}^{-1}$ ,

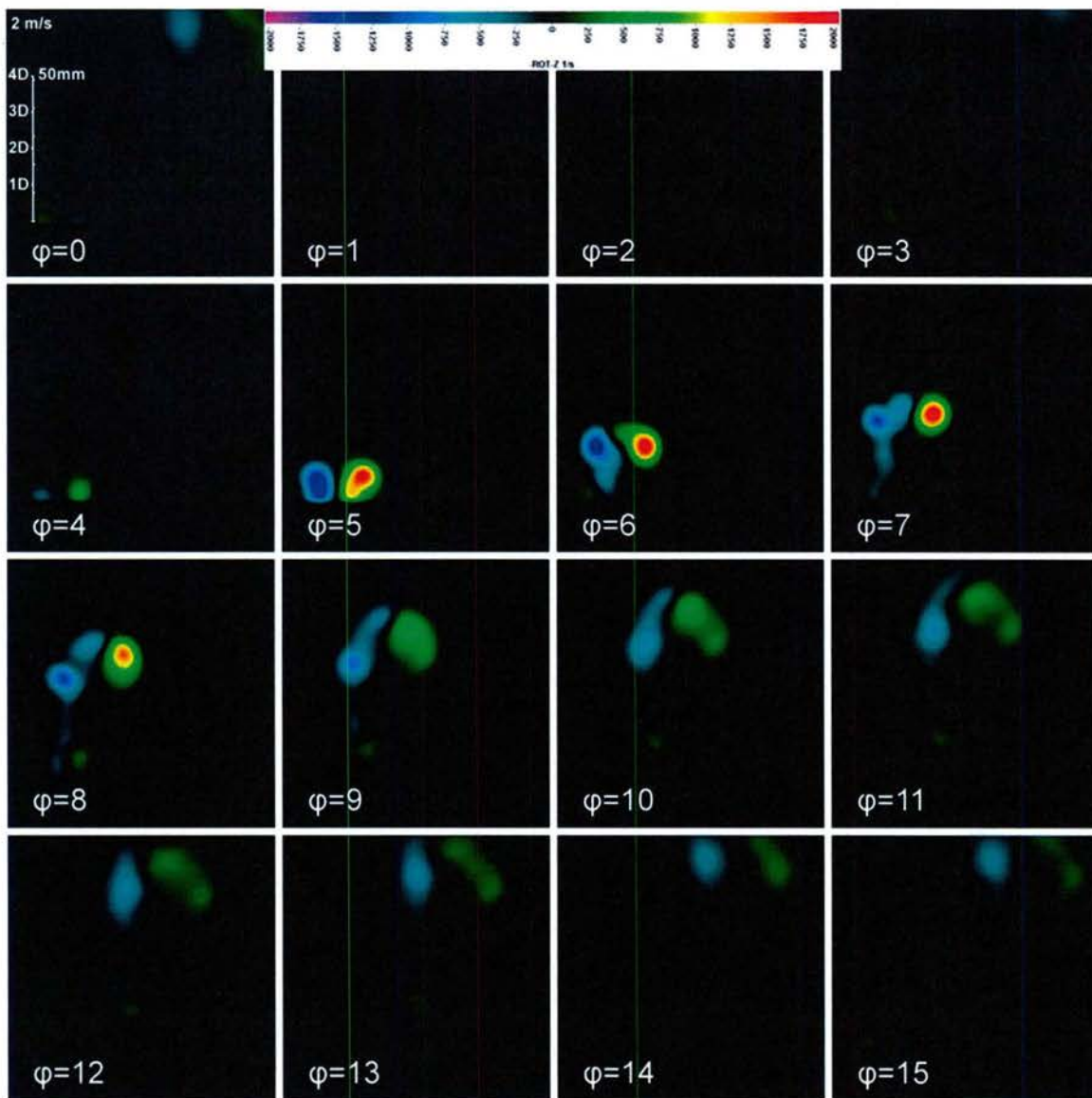


Fig. 25. Vorticity field for  $R = 0.39$ .

while the peak vorticity on the downstream side was  $\sim 2000 \text{ s}^{-1}$ . By  $\varphi=8$  the ring had pitched in the direction of crossflow. Beyond this point, the vortex structure quickly diminished in vorticity and lost much of its translational velocity in the  $y$ -direction.

In Fig. 25 the phase in which ingestion began is difficult to determine. Because the crossflow was sufficient to create appreciable vorticity in the boundary layer, it was no longer possible to use the appearance of positive vorticity at the upstream edge to indicate an influx of fluid. Instead, negative vorticity at the trailing edge was used. It was most likely that ingestion first occurred at  $\varphi=11$ . As with the  $R = 0.19$  case, the ingestion concluded at  $\varphi=2$ , with peak vorticity at  $\varphi=15$ . One noteworthy behavior in Fig. 25 that was not observed in the quiescent and  $R = 0.19$  cases is a curious region of positive vorticity at the leading edge of the orifice at  $\varphi=6$ . Also new in this case was a wake composed of alternating vorticities, which moved out of the field of view through almost purely translational motion.

The vorticity field for the  $R = 0.60$  case is shown in Fig. 26. In general, this case was similar to the two previous cases with the growth of vorticity in  $\varphi=4$  and the vortex structure convection in  $\varphi=6$ . The vorticity in the upstream portion of the structure from  $\varphi=3$  through  $\varphi=7$  appeared considerably diminished in comparison to the lower  $R$ -value cases. The vertical component of the ring velocity was also considerably lower. Furthermore, the ring pitched in the upstream direction more dramatically than in the lower  $R$ -value cases. At  $\varphi=8$ , the vortex structure appeared to be breaking up three orifice diameters from the hull. In the following phases, vorticity is amorphous and by  $\varphi=15$ , it is nearly washed out of the field of view.

As previously observed in the  $R = 0.39$  case, the ingestion phase began at  $\varphi=11$  and concluded at  $\varphi=2$ , with maximum vorticity at  $\varphi=15$ . During the early phases of ingestions, vorticity over the trailing edge of the orifice was less pronounced than in previous cases.

The wake for the  $R = 0.60$  case is more complicated than the lower  $R$ -value cases, showing stratification of vorticity in the streamwise as well as normal direction. The trailing vorticity visible in  $\varphi=5$  became separated from the vortex structure as it pitched into the crossflow. As this happened in  $\varphi=6$  and 7, there were two new regions of vorticity produced at the orifice, of the same sign as the vortex itself. These two regions then also pitched towards the direction of the crossflow, and moved downstream at a velocity comparable to the vortex.

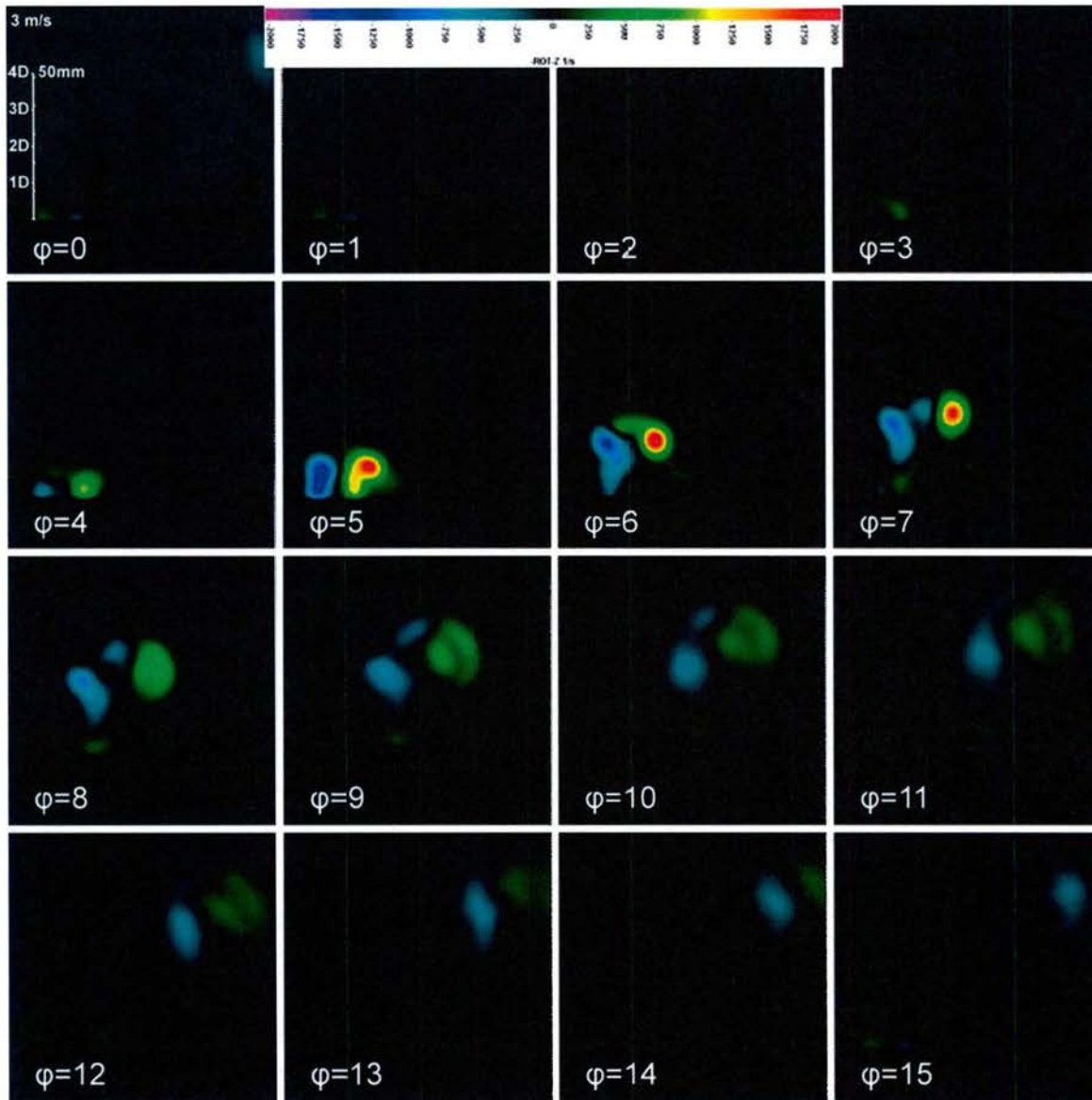


Fig. 26. Vorticity field for  $R = 0.60$ .

The vorticity field for the  $R = 0.81$  case is presented in Fig. 27. As in previous cases, the vorticity strengthened through  $\varphi=5$ , but the discrepancy between the leading and trailing regions was greater still, with peak upstream vorticity approximately 60% of the peak downstream value. By  $\varphi=5$  the vortex was pitching into the crossflow, and by  $\varphi=6$  it had pitched approximately  $20^\circ$ . The ring structure can be seen breaking up at roughly two orifice diameters from the hull at  $\varphi=7$ . Beyond this, the ring had broken into two diffuse regions of opposing vorticity. The upstream region assumed a crescent shape conforming to the circular downstream region. The two regions both wash out of the field of view in  $\varphi=13$ , roughly three orifice diameters from the surface.

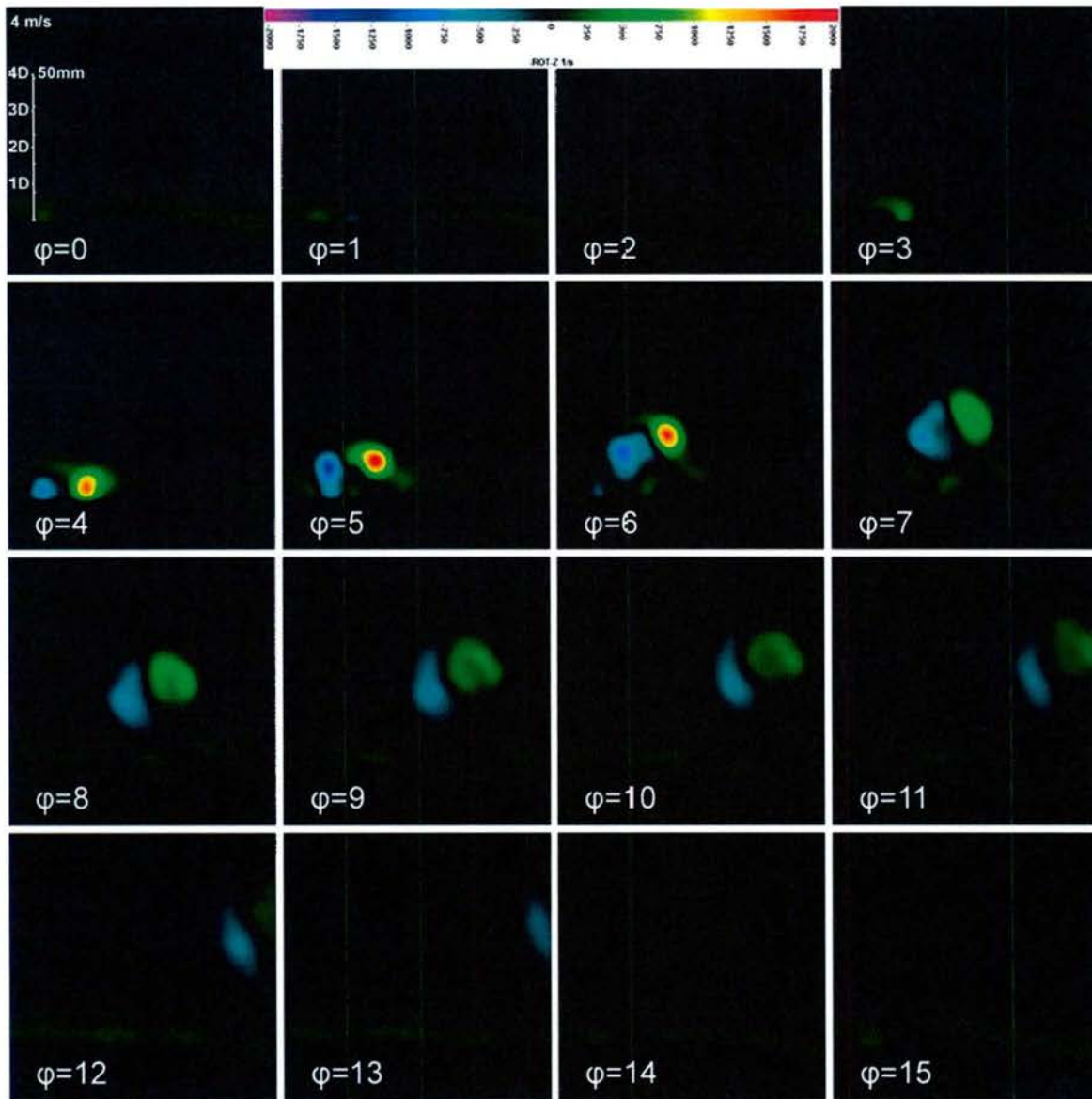


Fig. 27. Vorticity field for  $R = 0.81$ .

Finally, the vorticity field for the  $R = 0.96$  case is presented in Fig. 28; this was the highest crossflow case examined with PIV. As with all other cases, the outstroke began with the first appearance of negative vorticity at the upstream edge. This vorticity increased through  $\phi=5$ , where the negative vorticity appeared to be approximately 50% of the positive vorticity. At this point, the ring had already pitched nearly  $45^\circ$ . By  $\phi=6$ , the ring moved downstream but appeared unstable with diminished vorticity in the core. The wake in this case is fairly unremarkable except that the trailing vorticity behind the vortex core never separated away from the primary structure.

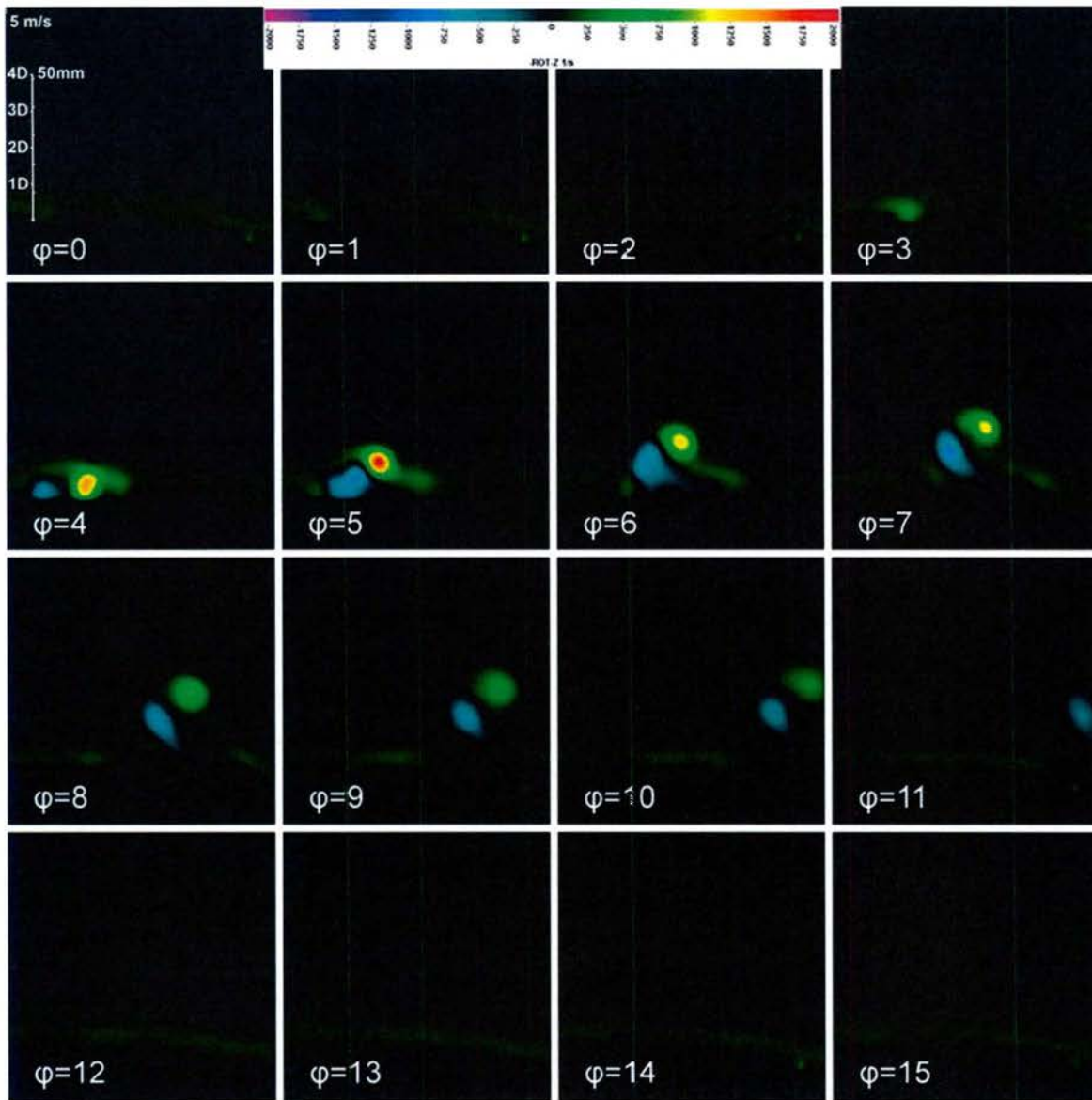


Fig. 28. Vorticity field for  $R = 1.05$ .

The locations of maximum vorticity for  $R$ -values as high as 0.60 were extracted from the vorticity fields and are presented in Fig. 29. Blue data points represent the upstream (left) portion of the ring structure ( $\omega < 0$ ) and red data points represent the downstream (right) portion of the ring structure ( $\omega > 0$ ). The lowest  $y/D$  values correspond to the  $\phi=6$  phase, the rest of the data come from the following phases. These plots show that with increasing crossflow velocity, there was a greater tendency for the vortex structure to pitch into the crossflow. It was also observed, based on the spacing between phases, that there was considerable decrease in the convection of the structure at higher crossflow velocities.

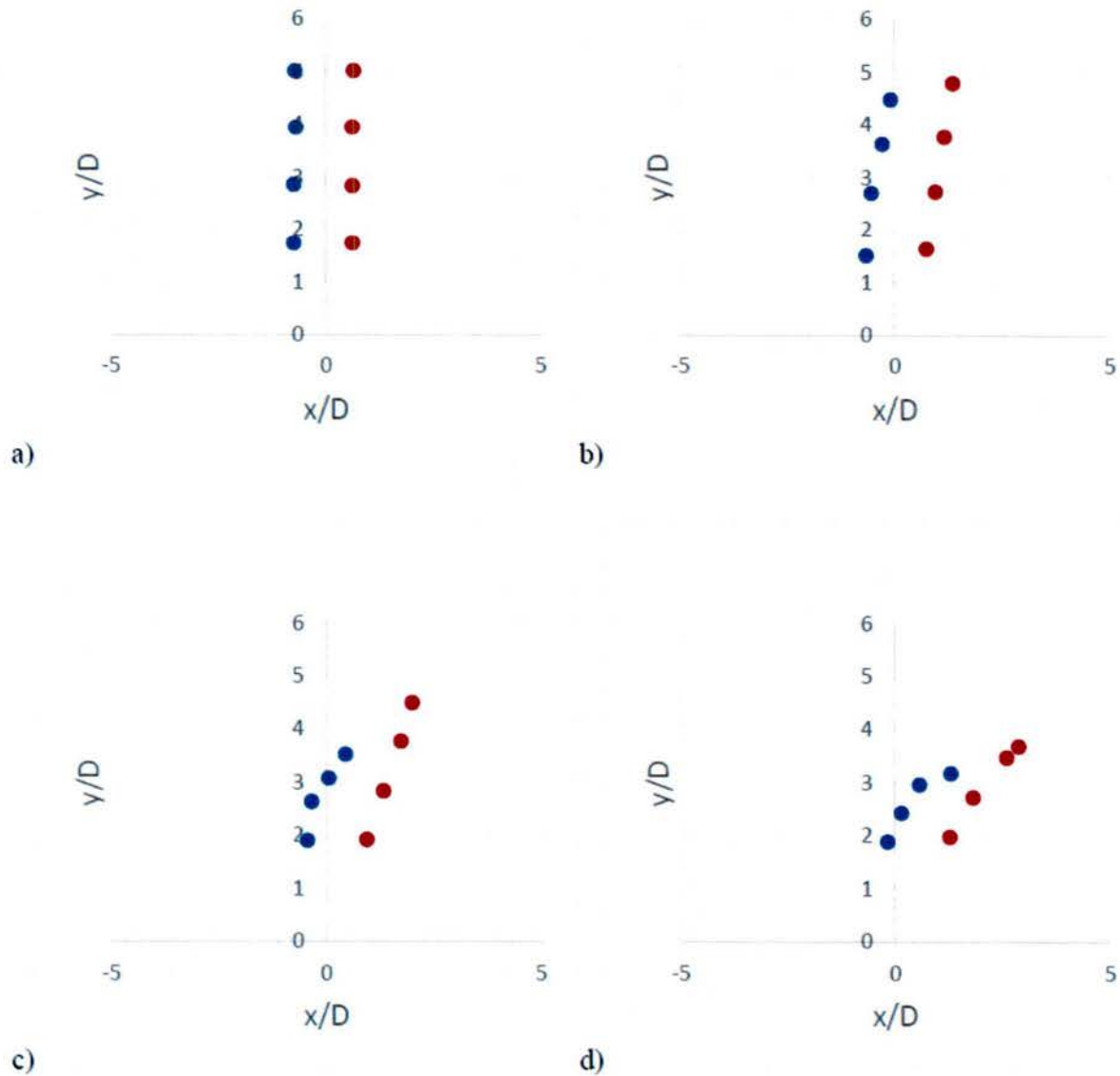


Fig. 29. Vortex core advancement; (a)  $R = 0$ , (b)  $R = 0.19$ , (c)  $R = 0.39$ , (d)  $R = 0.60$ .

### Ventilated Cavity Case

Thrust measurements were also carried out for the case of a ventilated cavity partially enclosing the model vehicle. The cavity closed upstream of the orifice. Three different gas ventilation rates of 50, 100, and 200 slpm were considered. Given the unsteady nature of the flow near the closing of the cavity, the measurements were quite noisy in general. Regardless of this, the data still offer insight, especially for the lower crossflow velocity cases.

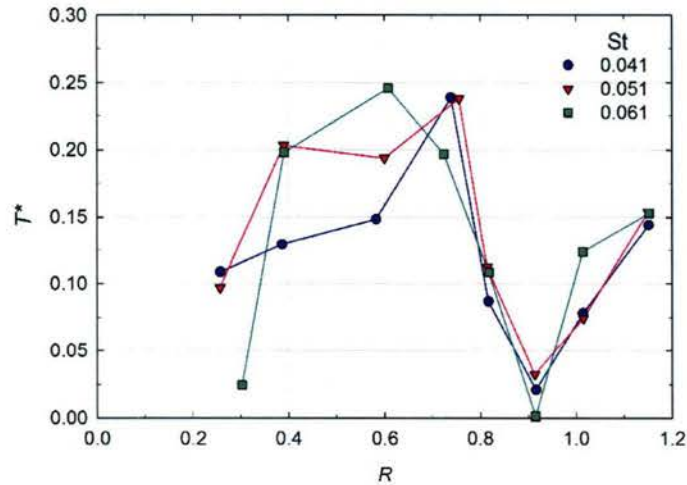


Fig. 30. Scaled thrust as a function of crossflow velocity ratio with a 50 slpm ventilation rate.

Scaled thrust is plotted in Fig. 30 as a function of crossflow velocity ratio for Strouhal numbers of 0.041, 0.051, and 0.061. Due to the large variation of the thrust during each run, all data points at each  $R$  have overlapping error bars. However, it is conceivable that the measurements cumulatively show trends for lower crossflow velocity ratios at the lower (50 slpm) ventilation rate. Even though the largest scaled thrust of  $\sim 0.25$  for the low ventilation rate is comparable to the fully-wetted case, the trend of increasing thrust prior to the crossflow velocity ratio of 0.75 is opposite of that for the fully-wetted cases where thrust continuously decreased with  $R$ . At  $R \approx 0.9$ , scaled thrust dropped to very small values. As  $R$  increased further,  $T^*$  began to increase again, climbing to approximately 0.15 for the highest  $R \approx 1.2$ .

For the 100 slpm intermediate ventilation rate, Fig. 31 below shows consistently positive scaled thrust values across the entire  $R$  range. The lowest crossflow velocity, corresponding to  $R \approx 0.7$ , shows  $T^*$  values that are greater than the scaled thrust for the fully-wetted case at the same Strouhal number. It is difficult to discern any distinct trend in the data, but in general, the thrust appeared to increase with the crossflow velocity ratio  $R$ . At the largest crossflow velocity ( $R = 1.25$ ) and the intermediate ventilation rate, the scaled thrust significantly exceeded the values associated with the fully-wetted case at the same  $R$ . The reason behind the disparity between the partial cavity and fully-wetted case is not clear at present; however, a change in the flow structure rather than the increased thrust is suspected.

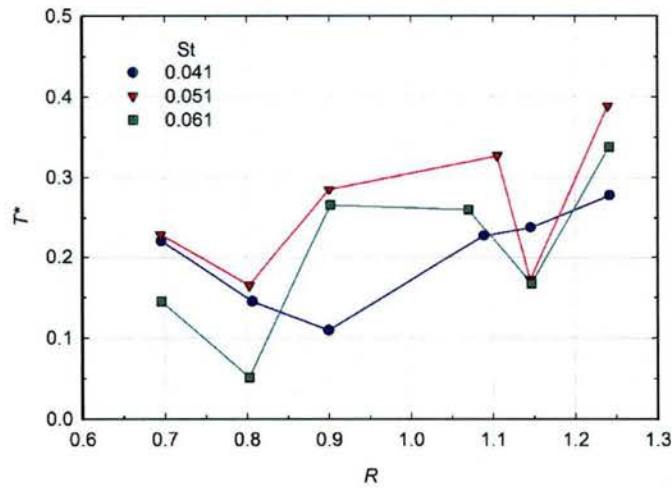


Fig. 31. Scaled thrust as a function of crossflow velocity ratio with a 100 slpm ventilation rate.

Scaled thrust for the highest ventilation rate of 200 slpm is presented in Fig. 32. Due to higher ventilation rate, crossflow velocity had to be increased and thus  $R$  ranges from one to about 1.6 for this ventilation rate. For the largest crossflow velocity, scaled thrust was negative for all three Strouhal numbers. For the lower crossflow velocities, thrust is positive except at  $R \approx 1.14$ . The sharp dip at this crossflow velocity ratio is consistent with a similar dip in  $T^*$  with the intermediate ventilation rate. In general,  $T^*$  decreased as  $R$  increased for the highest ventilation rate and this range of crossflow velocity ratios. Again, the reasons for the observed trend is not clear at present.

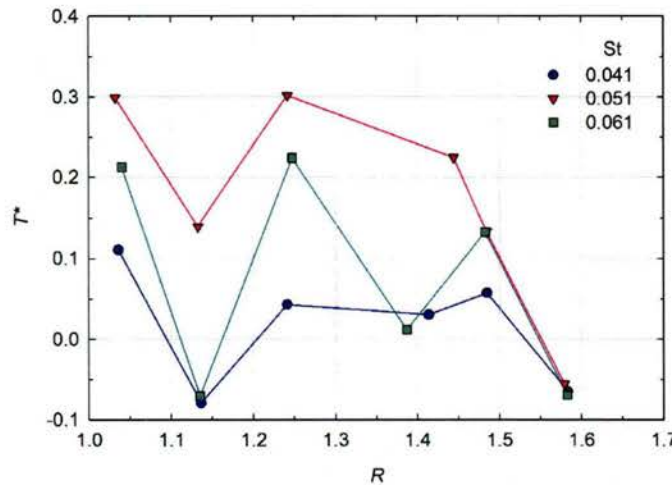


Fig. 32. Scaled thrust as a function of crossflow velocity ratio with a 200 slpm ventilation rate.

High speed video was also recorded for  $f = 20$  Hz ( $St = 0.051$ ) for various crossflow velocity ratios and the three ventilation rates. Certain noteworthy observations were found during the ingestion phase, and thus sequences of images are presented in time steps of 1 ms for the various crossflow velocities and ventilation rates.

The case of  $R \approx 0.4$  (nominal 2 m/s crossflow velocity) and ventilation rate of 50 slpm is shown in Fig. 33. From this image set, it can be seen that the near wall region contained many bubbles shed from the ventilated cavity upstream. Examination of the images closely revealed that the thruster ingested some of the ventilated gas (note the elongation of bubbles in the third image). During the expulsion phase, the vortex ring became turbulent immediately and had prominent cavitation in its core. As it convected, the cavitating ring pitched into the crossflow. The ring contorted and was unstable as it left the field of view. In some cases, the ring broke up completely within a few orifice diameters away from the hull. In the wake of the vortex ring, a cavitating region reminiscent of the vorticity in the fully-wetted  $R = 2.54$  case can be observed.



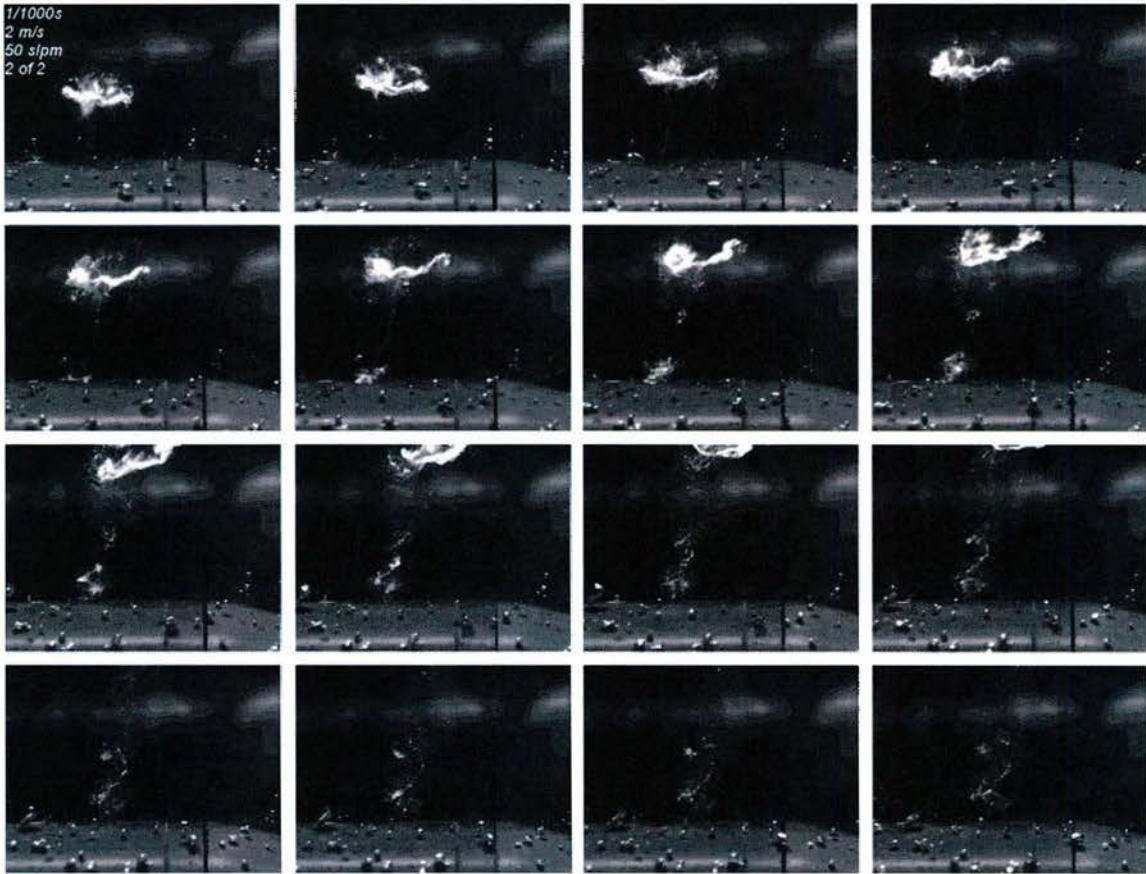


Fig. 33. Flow visualization for the low (50 slpm) ventilation rate at  $R \approx 0.4$ .

Fig. 34 shows the  $R \approx 0.5$  case with the low ventilation rate of 50 slpm. Similar to the previous case in Fig. 33, air bubbles are visible near the hull. These bubbles entered the orifice during the ingestion phase and contributed to a more prominent vortex ring core in the expulsion phase. Cavitation within the vortex core appeared first on the downstream edge of the ring. Shortly thereafter, cavitation was observed throughout the ring which then warped quickly into a saddle shape as it moved away from the hull. As the ring reached about 1.5 orifice diameters from the hull (6<sup>th</sup> row of images in Fig. 34), it began to pitch into the crossflow. At this same time, a stream of vapor (possibly due to cavitation) appeared in the trailing jet behind the vortex core. Following the collapse of this vapor cloud, the vortex ring became unstable and was torn apart in the crossflow.

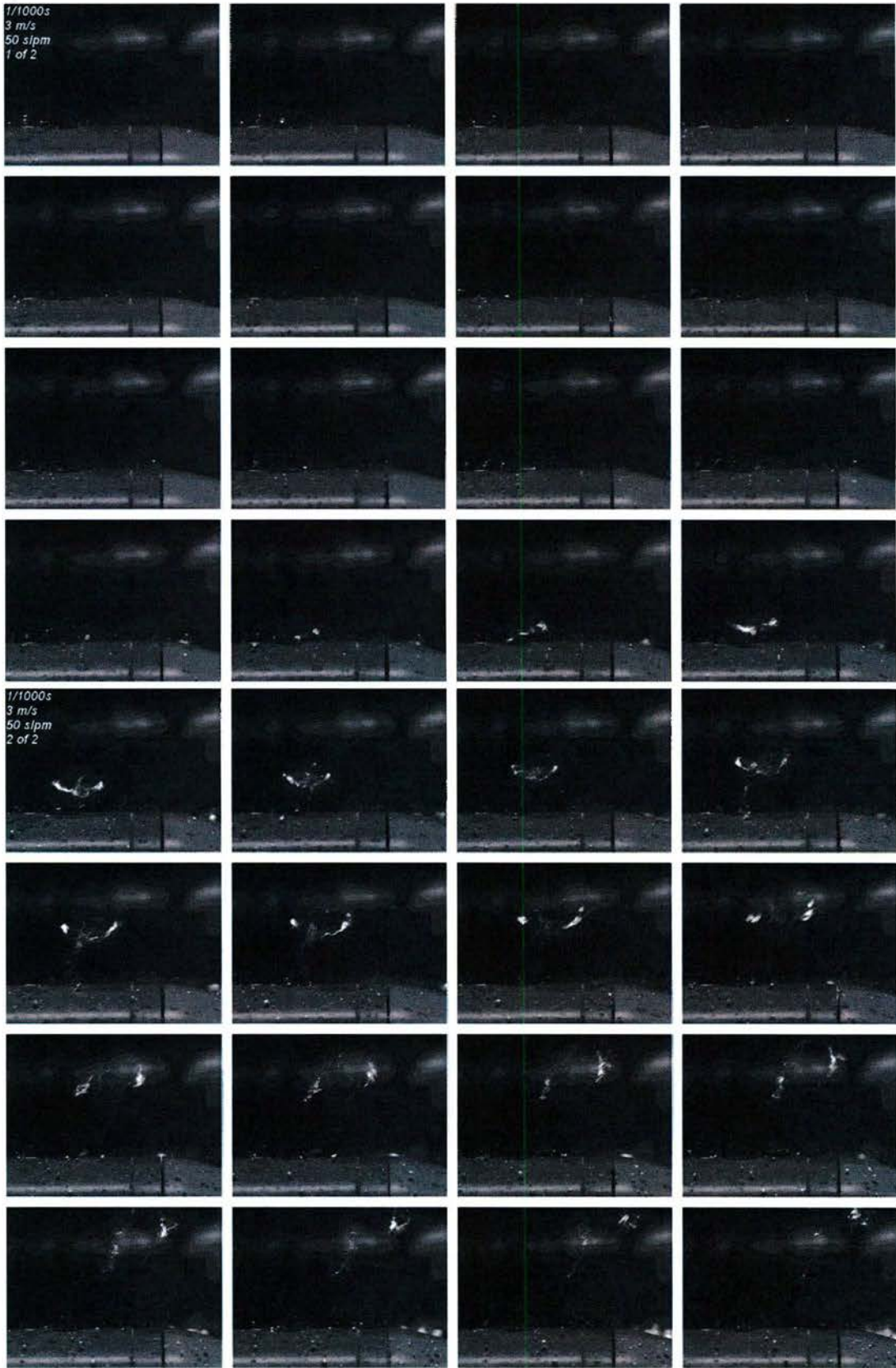


Fig. 34. Flow visualization for the low (50 slpm) ventilation rate at  $R \approx 0.5$ .

Direct flow visualization of the  $R \approx 0.8$  case with 50 slpm is presented in Fig. 35. At this tunnel speed and above, the ventilation gas from the cavitator began circulating with the tunnel flow and this caused haziness in the water; however, under close inspection it was observed that the amount of air in the boundary layer from the cavity at the bow is minimal compared to the lower  $R$  cases with the low ventilation rate. In the present case, the ring formed very similarly to the fully-wetted  $R = 0.8$  case. Once the ring was formed, it quickly pitched into the crossflow. At approximately 0.5 orifice diameters from the hull, two cavitating regions appear on the near and far edge of the orifice. These collapse as the ring began to pitch into the crossflow. The ring appeared to have completely broken up before reaching three orifice diameters from the hull.

Although not shown, the  $R = 0.8$  case with the moderate (100 slpm) ventilation rate was similar to the lower ventilation rate in Fig. 35. The only noteworthy differences were that the twin cavitation regions on the near and far edge of the orifice collapsed slightly earlier, and a small region of cavitation appeared briefly on the close edge of the orifice as the ring broke up.

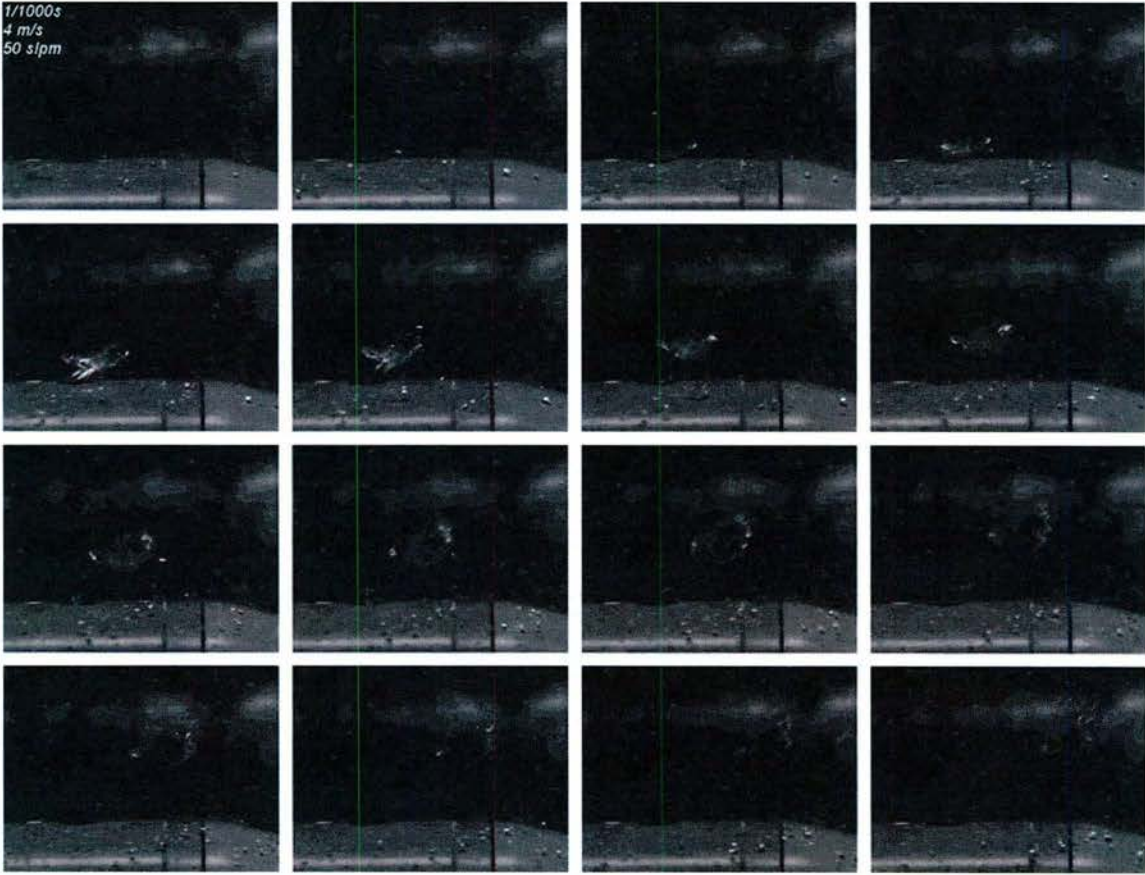


Fig. 35. Flow visualization for the low (50 slpm) ventilation rate at  $R \approx 0.8$ .

## Discussion

Measurements in the quiescent case revealed that thrust produced by the ZNMF thruster scales linearly with frequency for Strouhal numbers up to 0.04. For higher Strouhal numbers, the drop-off in thrust is mainly attributed to failure of the thruster to complete the pumping action across the entire stroke length. The observed linear scaling of thrust with frequency, as opposed to the frequency-squared scaling observed in harmonically driven ZNMF thrusters, is a result of the driving mechanism used in this design. Previous thrusters operating in aqueous environment have used motors and cams such that the pumping action follows a sinusoidal (or near-sinusoidal) motion; in these designs, the velocity of fluid leaving the orifice must increase to achieve higher frequencies as a result of compression of the waveform. The solenoid-driven thruster used here had essentially fixed outstroke and instroke profile; higher actuation frequencies resulted in a reduction of the time spent at the fully energized and fully resting positions. Figure 36 illustrates this difference in operation.

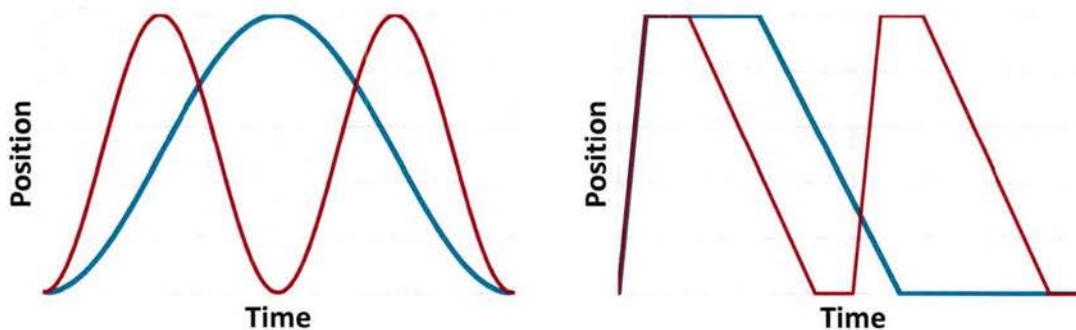


Fig. 36. Piston position for harmonic forcing (left) and pulsed forcing (right).

In the case of sinusoidal motion in Fig. 36, a doubling in frequency will increase the outward velocity at any point in the expulsion phase. Thus, the slug model predicts the thrust of a sinusoidally-driven thruster to scale with the square of frequency. This relationship exists because the momentum of the jet is the product of ejection velocity, approximately  $2 L f$ ; the number of ejections per time  $f$ ; and the mass of each fluid slug  $\rho L \pi D^2/4$ . This results in the scaling relationship  $T \sim D^2 L^2 f^2$ . Also recall that the characteristic velocity  $V_o$  of a ZNMF thruster is  $L/t^*$  which, as established, would be  $2 L f$  for the case of sinusoidal motion, but would be independent of frequency for a solenoid-driven thruster. For this reason, the thrust of a solenoid-driven thruster is expressed as  $T \sim D^2 L^2 f/t^*$ , a linear dependence on frequency. This relationship is intuitive when considering that in the case of a solenoid-driven thruster, we see

the repeated creation of discrete ring structures which have the same circulation and ejection velocity throughout the operational range of the mechanism. It is evident based on the data in Figs. 7 and 11 that there is virtually no influence from the preceding wakes for Strouhal numbers up to 0.04. For these reasons, frequency appeared to be indicative only of the number of discrete, momentum-producing expulsions in a given time frame.

Given the empirical correlation between scaled thrust and crossflow velocity in Eq. 7, we are left to explain the flow changes that bring about the observed decline in thrust with crossflow velocity. Inspection of the flow for crossflow velocity ratios of 0.6 and greater in Figs. 16 – 18 reveals an unusual structure; beginning at the near and far edges of the orifice, two elongated cavitation regions emerged, reaching towards and just inside the cavitating vortex ring core. At higher crossflow velocities, this phenomenon became quite pronounced (see Fig. 18) and was increasingly detrimental to the vortex ring structure.

It is hypothesized that the cavitation observed at the near and far edges of the orifice was a result of low pressure caused by the freestream flow forced to move around the slug behind the starting vortex ring. Based on the position of the ring core at the onset of the secondary cavitation region, it was determined that for crossflow velocity ratios of  $R = 0.6$  and  $0.8$ , this phenomenon occurred in the middle of the outstroke phase. The image in Fig. 37 shows the structure of the flow emerging from the orifice just before the appearance of described cavitation region. At this instant, the head of the expelled slug had already formed a vortex ring and the continued outflow of fluid was feeding the ring as it accelerates away from the hull. In Fig. 37,

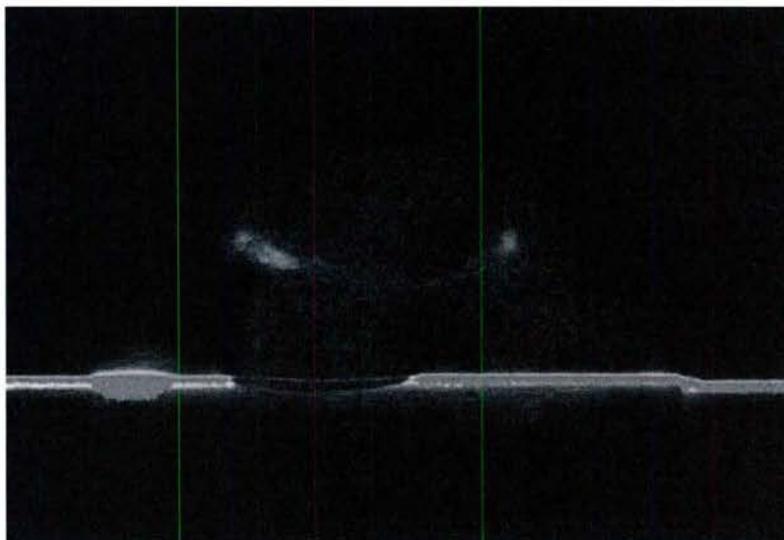


Fig. 37. Average of 50 raw PIV images for the fully-wetted case at  $R = 0.6$ .

the cavitating ring was far enough from the hull that the freestream flow existed beneath the ring. It is supposed that the deformation of crossflow streamlines in the vicinity of the fluid slug created localized pressure drop at the interface of the crossflow and slug. Furthermore, these low pressure regions would have low pressure footprints on the hull which result in forces opposite to the thrust produced by the fluid expulsion. It is the presence of these low pressure regions at the higher crossflow velocity ratios that are postulated to produce the reduction in the net force with increasing crossflow velocity.

Data collected for the ventilated cavitation case was primarily force data. For high ventilation rates and high crossflow velocities, systematic noise was too great to draw confident conclusions, but for the lowest ventilation rate the plots showed an interesting deviation from the fully-wetted case. In Fig. 30, a plot of scaled thrust is presented as a function of velocity ratio for three Strouhal numbers. The highest thrust did not occur at the lowest crossflow velocity; instead, thrust increased with increasing crossflow up to  $R = 0.61$ . It is supposed by observation of the high-speed video that the ingestion of air bubbles into the ZNMF thruster cavity may have caused lower thrust at low crossflow velocities. This phenomenon is best seen in Fig. 33. This two-phase ingestion not only lessened the mass of the extruded slug (thus decreasing momentum flux), but also introduced asymmetry to the ring structure, making its behavior more chaotic. Many of the vortex rings seen in low speeds ventilated cases broke up significantly earlier than in the corresponding fully-wetted cases. At  $R \geq 0.61$ , this contamination of the boundary layer was greatly reduced.

It was considered that this behavior might be credited to differences in gas leakage types. Based on the Campbell-Hilborne criteria, the type of leakage is determined by whether the product of the Froude number and cavitation number is less than or greater than one. In the case of  $\sigma Fr > 1$ , buoyancy is considerable and drives the cavity leakage to shed as twin vortex tubes. If  $\sigma Fr < 1$ , the cavity is nearly axisymmetric and gas is shed as toroidal vortices. However, calculating the cavitation numbers for all cases tested here revealed that the entirety of our experiments were conducted within the  $\sigma Fr > 1$  regime. Thus, it is reasonable to assert that the ZNMF thruster would not operate effectively within the  $\sigma Fr < 1$  regime, as leaked ventilation gas would be periodically swept over the model hull and disrupt the ZNMF thruster operation.

## Conclusions

The work presented here represents an investigation into a solenoid-driven zero-net-mass-flux thruster in crossflow for velocity ratios up to and beyond one. Thruster parameters were chosen with the intention of optimizing time-averaged momentum flux, as this work was intended to investigate the potential use of the thruster for maneuvering purposes. Within the scope of this research, the following conclusions can be drawn regarding generated loads, flow fields, and detrimental cavitation phenomena.

1. In the quiescent case, it was established that thrust varied linearly with operating frequency within the limitations of the thruster. This linear relationship is a result of individual expulsions being discrete impulse-generating events, which are not influenced significantly by preceding cycles.
2. In the fully-wetted crossflow experiments, it was demonstrated that the net thrust decreased nearly linearly with increasing crossflow velocity. An expression was developed to allow the estimation of net thrust as a function of the thruster operating parameters and crossflow velocity for crossflow velocity ratios as high as one.
3. Bowing of vortex ring structures seen with increasing crossflow may be explained by low pressure in the side regions, where secondary vortex structures spanned from the hull of the model to the inside edge of the vortex ring core.
4. Secondary vortex structures contributed to the early breakdown of the vortex ring structure in high crossflow velocity cases, where cavitation in the secondary structure was more intense.
5. The thruster performance was severely inhibited by the ingestion of air bubbles in the cases with a ventilated cavity that closed upstream of the thruster orifice.

## References

- Amitay M. and Glezer, A., "Controlled Transients of Flow Reattachment over Stalled Airfoils," *International Journal of Heat and Fluid Flow*, Vol. 23, 2002, pp. 690-699.
- Ayers, B., "The Control of Supercavitating Underwater Vehicles using Transverse Mounted Synthetic Jets," M.S. thesis, California State University Northridge, Northridge CA, 2015.
- Buren, T. V., Whalen E., and Amitay, M., "Vortex Formation of a Finite-Span Synthetic Jet: High Reynolds Number," *Physics of Fluids*, Vol. 26, 2014, 014101; doi: 10.1063/1.4859895.
- Cater, J. E. and Soria, J., "The evolution of round zero-net-mass-flux jets." *Journal of Fluid Mechanics*, Vol. 472, 2002, pp. 167-200.
- Chang, Y. K. and Vakili, A. D., "Dynamics of vortex rings in crossflow," *Physics of Fluids*, Vol. 7, 1995, pp. 1583–1597.
- Chaudhari, M., Puranik B., and Agrawal, A., "Head transfer characteristics of synthetic jet impingement cooling," *International Journal of Heat and Mass Transfer*, Vol. 53, 2010, pp. 1057-1069.
- DeMauro, E. P., Leong, C. M., and Amitay, M., "Interaction of Synthetic Jet with Flow over a Low Aspect Ratio Cylinder," *Physics of Fluids*, Vol. 25, 2013.
- Eroglu, A. and Briedenthal, R. E., "Structure, penetration and mixing of pulsed jets in crossflow," *AIAA Journal*, Vol. 39, 2001, pp. 417–423.
- Gharib, M., Rambod, E., and Shariff, K., "A universal time scale for vortex ring formation," *Journal of Fluid Mechanics*, Vol. 360, 1998 , pp. 121–140.
- Glezer, A. and Amitay, M., "Synthetic Jets," *Annual Review of Fluid Mechanics*, Vol. 34, 2002, pp. 503-529.
- Glezer, A., "Some aspects of aerodynamic flow control using synthetic-jet actuation," *Philosophical Transactions of the Royal Society*, Vol. 369, 2011, pp. 1476-1494.
- Gopalan, S., Abraham, B. M., and Joseph Katz, J., "The structure of a jet in cross flow at low velocity ratios," *Physics of Fluids*, Vol. 16, No. 6, 2004, pp. 2067-2087.
- James, R. D., Jacobs, J. W., and Glezer, A., "A round turbulent jet produced by an oscillating diaphragm," *Physics of Fluids*, Vol. 8, 1996, pp.2484-2495.
- Johari, H., "Scaling of fully pulsed jets in crossflow," *AIAA Journal*, Vol. 44, 2006, pp. 2719–2725.
- Kercher, D. S., Lee, J.-B., Brand, O., Allen, M. G., and Glezer, A., "Microjet Cooling

Devices for Thermal Management of Electronics," *Transactions on Components and Packaging Technologies*, Vol. 26, No. 2, 2003, pp. 359-366.

Kreig M. and Mohseni, K., "Incorporation of Novel Underwater Thrusters into Vehicle Control Systems," in IEEE International Conference on Robotics and Automation, Pasadena, CA, 2008.

Kreig, M., Pitty, A., Salehi, M., and Mohseni, K., "Optimal Thrust Characteristics of a Synthetic Jet Actuator for Application in Low Speed Maneuvering of Underwater Vehicles," in OCEANS, Proceedings MTS/IEEE, Piscataway NJ, 2005.

M'Closkey, R. T., King, J. M., Cortelezzi, L., and Karagozian, A. R., "The actively controlled jet in crossflow," *Journal of Fluid Mechanics*, Vol. 452, 2002, pp. 325–335.

Mahalingam, R., Rumigny N., and Glezer, A., "Thermal Management Using Synthetic Jet Actuators," *IEEE Transactions on Components and Packaging Technologies*, Vol. 27, No. 3, 2004, pp. 439-444.

Maldonado, V., Farnsworth, J., Gressick, W., and Amitay, M., "Active control of flow separation and structural vibrations of wind turbine blades," *Wind Energy*, Vol. 13, 2009, pp. 221-237.

Mejia, O. D. L., Moser, R. D., and Brzozowski, D. P., "Effects of Trailing-Edge Synthetic Jet Actuation on an Airfoil," *AIAA Journal*, Vol. 49, No. 8, 2011, pp. 1763-1777.

Mohseni, K., "Pulsatile vortex generators for low-speed maneuvering of small underwater vehicles," *Ocean Engineering*, Vol. 33, 2006, pp. 2209-2223.

Polisenburg-Thomas, A., Burdick, J., and Mohseni, K., "An Experimental Study of Voice-Coil Driven Synthetic Jet Propulsion for Underwater Vehicles," in OCEANS, proceedings MTS/IEEE, Piscataway NJ, 2005.

Sau, R. and Mahesh, K., "Dynamics and mixing of vortex rings in crossflow," *Journal of Fluid Mechanics*, Vol. 604, 2008, pp. 389–409.

Smith, B. L. and Glezer, A., "The formation and evolution of synthetic jets," *Physics of Fluids*, Vol. 10, No. 9, 1998, pp. 2281-2297.

Tamburello D. A. and Amitay, M., "Active Control of a Free Jet using a Synthetic Jet," *International Journal of Heat and Fluid Flow*, Vol. 29, 2008, pp. 967-984.

Vasile J. D. and Amitay, M., "Interaction of a Finite-Span Synthetic Jet near the Tip of a Sweptback Wing," *Physics of Fluids*, Vol. 27, 2015, 067102; doi: 10.1063/1.4921844.

Woo G. T. K. and Glezer, A., "Controlled transitory stall on a pitching airfoil using pulsed actuation," *Experiments in Fluids*, Vol. 54, 2013, 1507.

## **Publications**

Ayers, B. and Johari, H., "Thrust of a Zero-Net-Mass-Flux Actuator in Aqueous Crossflow," 54<sup>th</sup> AIAA Aerospace Sciences Meeting, San Diego, CA, January 2016, paper 2016-0589. Also, in preparation for submission to the *AIAA Journal*.

Ayers, B., Henoch, C., and Johari, H., "Flow Field of a Zero-Net-Mass-Flux Thruster in Crossflow," in preparation for submission to an archival journal.

## **Presentations**

Ayers, B., Henoch, C., and Johari, H., "Experiments on the Thrust of a Synthetic Jet in Crossflow," 67<sup>th</sup> Annual Meeting of the APS-DFD, San Francisco, CA, Nov. 2014.

Ayers, B., Henoch, C., and Johari, H., "Modeling of a Zero-Net-Mass-Flux Actuator for Aqueous Media," 68<sup>th</sup> Annual Meeting of the APS-DFD, Boston, MA, Nov. 2015.

Two presentations at ONR-ULI review meetings.

## **Graduate Student**

Mr. Bradley Ayers was the graduate student on this project, and he completed his M.S. in Mechanical Engineering from California State University, Northridge in August 2015.

## **Navy Lab Mentor**

Dr. Charles W. Henoch, Hydrodynamics Branch, Naval Undersea Warfare Center, Newport, RI.